CDF/ANAL/EXOTIC/PUBLIC/11116
Version 1.1

Search for the Fermiophobic Higgs Boson Using the $3\gamma + X$ Final State in CDF Run II Data from 9.2 fb^{-1} of $p\bar{p}$ Collisions

The CDF Collaboration
URL http://www-cdf.fnal.gov
(Dated: September 15, 2014)

We search for the fermiophobic Higgs boson (h_f), in the context of the two Higgs doublet model (type I), using $3\gamma + X$ events in $p\bar{p}$ collisions at $\sqrt{s} = 1.96$ TeV. In this model, the h_f is assumed to be produced in association with the charged Higgs boson ($H^{\pm}$) followed by the $H^{\pm}$ decaying to $h_f W^*$ and both of the two h_f's decaying to 2γ. The data were collected with the CDF-II detector at the Fermilab Tevatron collider and correspond to an integrated luminosity of 9.2 fb^{-1}. The number of backgrounds is estimated to be 2.96 ± 0.94 events, where the direct triphoton production dominates the contribution. The expected numbers of signal events are estimated for a set of the h_f and $H^{\pm}$ mass combinations. For example, it is 35 events for the h_f mass 75 GeV/c^2 and the $H^{\pm}$ mass 120 GeV/c^2, with H^0 mass = 500 GeV/c^2, A^0 mass = 350 GeV/c^2, and $\tan\beta = 10$. The observed number of events in the data is 5. From these results, we obtain the limits on $\sigma(p\bar{p} \to h_f H^{\pm}) \times \mathcal{B}(H^{\pm} \to h_f W^*) \times [\mathcal{B}(h_f \to 2\gamma)]^2$ at the 95% confidence level. By comparing with the theoretical cross sections, the cross section limits are translated to h_f mass constraints for a given $m_{H^{\pm}}$, which are collectively represented as a rather large excluded region on the m_{h_f} vs. $m_{H^{\pm}}$ plane.

I. INTRODUCTION

Understanding the mechanism of electroweak gauge symmetry breaking (EWSB) is considered, for a long time, to be one of the most important milestones and major challenges in the elementary particle physics. In the Standard Model (SM), a doublet of complex scalar fields, the Higgs fields, are introduced to explain the EWSB and the origin of particle masses via a spontaneous EWSB, the so-called the Higgs mechanism.

The experiments using the Large Hadron Collider (LHC) at CERN discovered a scalar boson in 2012 [1]. The results support that the EWSB be indeed related to a scalar boson. Moreover, it was recently reported that the new particle actually coupled to fermions [2], which is also expected for the SM Higgs boson. The whole picture of the EWSB is, however, yet to be investigated. Even if the new particle is confirmed to be the SM Higgs boson, it does not mean that, for example, there are no other Higgs bosons, and there could be multiple Higgs bosons in the underlying fundamental physics. It is thus still necessary to continue testing various senarios as long as they are not explicitly excluded.

A minimal multiple-Higgs model is the "two Higgs doublet model" (2HDM). The resulting particle spectrum consists of two charged Higgs bosons H^+, H^- and three neutral members h^0, H^0 and A^0. The fermiophobic Higgs boson, which signifies very suppressed or zero couplings to the fermions, may arise in a particular version of the 2HDM called type I.

A. Models with fermiophobia

The 2HDM (type I) was first proposed in [3]. In this model, one Higgs doublet (Φ_2) of the $SU(2) \otimes U(1)$ gauge group couples to all the fermion types, while the other doublet (Φ_1) does not. Both couple to the gauge bosons via the kinetic term in the Lagrangian. One vacuum expectation value (v_2) gives masses to all the fermion types, while the gauge bosons receive their masses from both the v_1 and v_2.

Due to the mixing in the CP-even neutral Higgs sector, both the CP-even eigenstates h^0 and H^0 can couple to the fermions. The fermionic coupling of the lightest CP-even Higgs boson h^0 takes the form

$$h^0 f\bar{f} \sim \frac{\cos\alpha}{\sin\beta}\,,$$

where the f is any fermion, the α is the mixing angle in the neutral Higgs sector h^0 and H^0, and the β is defined by

$$\tan\beta = \frac{v_2}{v_1}\,.$$

Small values of the $\cos\alpha$ would seriously suppress the fermionic coupling, and in the limit

$$\cos\alpha \to 0\,,$$

the coupling $h^0 f\bar{f}$ would vanish, giving rise to the fermiophobia and the h^0 is called a fermiophobic Higgs (h_f) [4].

The main decay mode of the h_f is

$$h_f \to 2\gamma$$

for $m_{h_f} \lesssim 95$ GeV/c^2. The branching fraction ($\mathcal{B}$) is near 100% for $m_{h_f} \lesssim 80$ GeV/c^2, decreasing to 50% at $m_{h_f} \simeq 95$ GeV/c^2, and to 1% at $m_{h_f} \simeq 145$ GeV/c^2. In contrast, the $\mathcal{B}(\phi^0 \to 2\gamma) \simeq 0.22\%$ is the largest value in the SM, where the ϕ^0 represents the SM Higgs boson. We shall be focusing on the possibility of a light h_f,

$$m_{h_f} \lesssim 100 \text{ GeV}/c^2\,,$$

for which the photonic decay mode always has a large $\mathcal{B}$.

B. Previous searches

The h_f had been searched for at the LEP, Tevatron, and the LHC experiments. A conventional h_f production and decay process at e^+e^- colliders is

$$e^+e^- \to Z^* \to h_f(\to 2\gamma)Z\,,$$

and at hadron colliders

$$q\bar{q}' \to V^* \to h_f(\to 2\gamma)V \,,$$

with the dominant contribution coming from $V = W^{\pm}$.

The OPAL and DELPHI collaborations also searched for the process

$$e^+e^- \to h_f(\to 2\gamma)A^0 \,,$$

and the L3 collaboration considered

$$e^+e^- \to h_f(\to WW^*)Z$$

as well. The LEP ruled out regions on the plane

$$R \times \mathcal{B}(h_f \to 2\gamma) \quad \text{vs.} \quad m_{h_f},$$

where the R is defined by

$$R = \frac{\sigma(e^+e^- \to h_f Z)}{\sigma(e^+e^- \to \phi^0 Z)} \,.$$

In the benchmark scenario of the $R = 1$ and assuming $\mathcal{B}(h_f \to 2\gamma)$ given by [5, 6], each of the LEP collaborations, OPAL, DELPHI, ALEPH, and L3, derived a limit of $m_{h_f} \gtrsim 100$ GeV/c^2 at the 95% confidence level (C.L.). A combination of the results [7] yielded a lower bound

$$m_{h_f} > 109.7 \text{ GeV}/c^2 \,.$$

In the Tevatron Run II, the lower limit on the m_{h_f} from the combined CDF and DØ analyses [8] was

$$m_{h_f} > 119 \text{ GeV}/c^2$$

at the 95% C.L., where the processes

$$q\bar{q}' \to V^* \to h_f(\to \gamma\gamma)V \,, \qquad q\bar{q}' \to V^* \to h_f(\to WW^*)V \,,$$

$$q\bar{q}' \to q\bar{q}' h_f(\to 2\gamma) \,, \qquad q\bar{q}' \to q\bar{q}' h_f(\to WW^*) \,,$$

were considered in the analysis.

Both the ATLAS and the CMS collaborations searched for

$$q\bar{q}' \to V^* \to h_f(\to \gamma\gamma)V \,, \qquad q\bar{q}' \to q\bar{q}' h_f(\to 2\gamma) \,,$$

and obtained the results

$$m_{h_f} \notin 110\text{–}118 \,,\, 119.5\text{–}121.0 \text{ GeV}/c^2 \,,$$

and

$$m_{h_f} \notin 110\text{–}147 \text{ GeV}/c^2 \,,$$

respectively [9].

All these mass limits assumed that the $h_f VV$ coupling was of the same strength as the SM coupling $\phi^0 VV$, which in general would not be the case for the h_f in a realistic model such as the 2HDM (type I). The condition for the fermiophobia ($\cos\alpha \to 0$) causes the coupling $h_f VV$ to be suppressed by a factor

$$h_f VV \sim \sin^2(\beta - \alpha) \to \cos^2\beta \equiv \frac{1}{1 + \tan^2\beta} \,.$$

Taking $\tan\beta > 3$ (10) implies a strong suppression of ~ 0.1 (0.01) with respect to the coupling $\phi^0 VV$. It is not difficult to see that such a suppression in the R would permit a light h_f with the mass of ~ 80 (50) GeV/c^2, thus sizable regions of the $R \times \mathcal{B}(h_f \to \gamma\gamma)$ vs. m_h plane remain unexcluded. One could therefore imagine a scenario of a very light h_f ($m_{h_f} \lesssim 100$ GeV/c^2) which eluded the previous searches at the LEP, Tevatron, and LHC experiments.

At the Tevatron, other production mechanisms are available that could allow the discovery of the h_f even in the region where the process $q\bar{q}' \to h_f V$ is suppressed.

C. Signature of signal events

We introduce a production process which may offer sizable rates of the h_f even in the region where the coupling $h_f VV$ is very suppressed. We consider [10]

$$q\bar{q}' \to W^* \to h_f H^\pm \, .$$

A quark-antiquark annihilation produces a h_f in association with a $H^\pm$ via an intermediate W boson. This process makes use of the Higgs-Higgs-vector boson coupling,

$$H^\pm h_f W^\pm \sim \sin\beta \, ,$$

in the 2HDM (type I), providing non-negligible cross sections in the large $\tan\beta$ regions.

We then use the cascade decays

$$H^\pm \to h_f W^*$$

which may have large $\mathcal{B}$'s. The large $\mathcal{B}$ can arise since the coupling of $H^\pm$ to all the fermions scales as

$$H^\pm f f' \sim \frac{1}{\tan\beta} \, ,$$

and thus for moderate to large $\tan\beta$, $\tan\beta = 3$ and 30 as discussed in [10] for example, even the three-body decays (i.e. with V^*) can have sizable or dominant $\mathcal{B}$'s. Moreover, the double h_f production may result in a distinctive 4γ topology and the multi-photon signature should have an advantage of very small background rates.

In this study, we perform a search for the fermiophobic Higgs using the $3\gamma + X$ final state emerging from the process

$$p\bar{p} \to h_f H^\pm \to h_f \, (h_f W^*) \to (2\gamma)(2\gamma) + X.$$

In Fig. 1 is shown the cross section

$$\sigma(p\bar{p} \to h_f H^\pm) \times \mathcal{B}(H^\pm \to h_f W^*) \times [\mathcal{B}(h_f \to 2\gamma)]^2 \, .$$

A Feynman diagram of this process is shown in Fig. 2.

In the past, the DØ collaboration performed this type of analysis using their 0.83 pb^{-1} of data [11]. They found the data consistent with the background expectation and obtained mass limits on the m_{h_f} for benchmark $H^\pm$ mass-points of 100 GeV/c^2 and 150 GeV/c^2 assuming $\tan\beta = 3$ and $\tan\beta = 30$. For example,

$$m_{h_f} > 80 \text{ GeV}/c^2 \text{ at the 95\% C.L.}$$

for $m_{H^\pm} = 100$ GeV/c^2 and $\tan\beta = 30$.

II. DATA SAMPLES AND EVENT SELECTION

This analysis is based on the data collected with the CDF-II detector between February 2002 and September 2011, corrsponding to and integrated luminosity of 9.2 fb^{-1} after the run filtering for good detector conditions. Detailed descriptions of the CDF-II detector can be found in [12].

The diphoton triggers with an E_T threshold of 12 GeV and a triphoton trigger with an E_T threshold of 10 GeV are used to create the initial data sample for our analysis. We then select events with at least 3 photons with $E_T > 15$ GeV. The photons must be found in the central detector ($|\eta| < 1.1$) and within fiducial regions of the sub-detectors. They are also required to be isolated in terms of the calorimeter and track cone-isolation. We then apply cuts for photon identification based on the EM shower profile. We veto photon candidates if there is an additional nearby cluster found in the EM shower-max strip detector to reject $\pi^0/\eta^0 \to 2\gamma$ decays. In the case that more than 3 photon-candidates are found in a given event, we sort them from the one with having the largest E_T, then pick up the first 3 photon-candidates for further analysis.

III. SIGNAL EFFICIENCY AND ITS UNCERTAINTY

A. Signal efficiency

The trigger efficiency is taken to be 100% for our combination of triggers and high E_T photons passing our selection cuts. The rest of the detection efficiency is estimated as a function of h_f and $H^{\pm}$ masses using the PYTHIA Monte Carlo (MC) data, with at least 40000 events for each mass point. The h_f masses range from 10 GeV/c^2 to 105 GeV/c^2 at a typical increment of 10 GeV/c^2, and from 30 GeV/c^2 to 300 GeV/c^2 for the $H^{\pm}$ masses with 5–25 GeV/c^2 steps. For other parameters, we set $\alpha = \pi/2$ to ensure the fermiophobia ($\cos\alpha = 0$) and $\tan\beta = 10$ to be conservative compared to $\tan\beta = 30$ but still to sufficiently suppress the $h_f VV$ coupling and $H^{\pm}$ decays to fermions. The H^0 and A^0 masses are chosen to be large enough so as not to play in the $H^{\pm}$ decays. We set the H^0 mass = 500 GeV/c^2 and the A^0 mass = 350 GeV/c^2, but there is no strong reason for picking up these particular values.

The generated events are all passed through the full detector simulation. We estimate the efficiency by the following simple fraction:

$$\epsilon = \frac{\text{the number of Higgs-MC events passing the selection cuts}}{\text{the number of generated Higgs-MC events with } 4\gamma} \,. \tag{1}$$

The photon selection are not perfectly modeled in the simulation which are corrected for by appling the MC scale factors in the efficiency calculation. Figure 3 shows the signal efficiencies. Typically, the efficiencies are 0.1–1% when the m_{h_f} is smaller than 20 GeV/c^2, then rise to 15–20% as the m_{h_f} becomes large.

B. Systematic uncertainties

We take a systematic uncertainty of 2.7% per photon related to the efficiency for the photon selection, which is estimated by comparing EM shower modeling in MC and real data using the process $Z \to e^+e^-$. Since there are three photons we take the total systematic uncertainty to be $3 \times 2.7\% = 8.1\%$.

When a proton and an anti-proton collide, it is mostly a single sub-particle, a parton (quark or gluon) in the proton or anti-proton, that participates in the hard collision and produces a high center-of-mass energy event. The momentum fraction, described by parton distribution functions (PDFs), that is carried by each of the partons in the proton or anti-proton is not perfectly understood. It affects the kinematics of the outgoing final state particles. To estimate the magnitude of this effect on the detection efficiency we evaluate, event-by-event, the uncertainty of the probability for a given momentum fraction of the colliding parton using a "PDF-set" by the CTEQ collaboration (CTEQ-5L). As only the newer PDF-set version CTEQ-6M contains 90% confidence intervals for each eigenvector, the total uncertainty is estimated by reweighting the parton momenta of the original CTEQ-5L set and varying the PDFs using the uncertainties from CTEQ-6M. We get a relative uncertainty of 1% on the detection efficiency.

The initial state radiation (ISR) caused by a gluon radiating from an incoming quark or the final state radiation (FSR) from an outgoing quark can both make the E_T spectrum of the final state particles softer than the case without radiation. The variations of the ISR/FSR thus can cause the photon or the jets to be systematically more or less likely to pass the kinematic requirements. The effect carries a non-negligible theoretical uncertainty and is estimated by comparing results based on MC data generated with different values of MC parameters to control the ISR and FSR. Doing so we find a variation in the detection efficiency, taken to be the systematic uncertainty, of 2%.

We include the systematic uncertainty of the efficiency due to variations of the Q^2 scale. The variation observed by changing the scale from $0.25Q^2$ to $4Q^2$ is 3%.

IV. BACKGROUND ESTIMATION

There are two major sources of the background events. The first comes from the events in which jets are mis-identified as photons. The other source is the Direct Triphoton Production (DTP).

A. Background with mis-identified photons

QCD backgrounds to the $3\gamma + X$ final state contain at least one electromagnetic-like (EM-like) jets denoted here by j. There are 8 possible combinations of photons and jets: $\{\gamma,\gamma,\gamma\}$, $\{\gamma,\gamma,j\}$, $\{\gamma,j,\gamma\}$, $\{j,\gamma,\gamma\}$, $\{\gamma,j,j\}$, $\{j,\gamma,j\}$,

$\{j, j, \gamma\}$, and $\{j, j, j\}$, where the ordering in a combination is determined by the E_T. The 1st component can, in principle, contain the Higgs signal. The number of 3γ events that are produced can be obtained by solving eight linear equations:

$$\boldsymbol{n} = \boldsymbol{E}\boldsymbol{n}^* \qquad \left(n_i = \sum_{j=1}^{8} E_{ij} n_j^* \,, \quad i = 1, \cdots, 8 \right) \,,$$

or by writing the components explicitly,

$$\begin{pmatrix} n_{ppp} \\ n_{ppf} \\ n_{pfp} \\ n_{fpp} \\ n_{pff} \\ n_{fpf} \\ n_{ffp} \\ n_{fff} \end{pmatrix} = \begin{pmatrix} \epsilon_s\epsilon_s\epsilon'_s & \epsilon_s\epsilon_s\epsilon'_b & \epsilon_s\epsilon_b\epsilon'_s & \epsilon_b\epsilon_s\epsilon'_s & \epsilon_s\epsilon_b\epsilon'_b & \epsilon_b\epsilon_s\epsilon'_b & \epsilon_b\epsilon_b\epsilon'_s & \epsilon_b\epsilon_b\epsilon'_b \\ \epsilon_s\epsilon_s\bar{\epsilon'_s} & \epsilon_s\epsilon_s\bar{\epsilon'_b} & \epsilon_s\epsilon_b\bar{\epsilon'_s} & \epsilon_b\epsilon_s\bar{\epsilon'_s} & \epsilon_s\epsilon_b\bar{\epsilon'_b} & \epsilon_b\epsilon_s\bar{\epsilon'_b} & \epsilon_b\epsilon_b\bar{\epsilon'_s} & \epsilon_b\epsilon_b\bar{\epsilon'_b} \\ \epsilon_s\bar{\epsilon_s}\epsilon'_s & \epsilon_s\bar{\epsilon_s}\epsilon'_b & \epsilon_s\bar{\epsilon_b}\epsilon'_s & \epsilon_b\bar{\epsilon_s}\epsilon'_s & \epsilon_s\bar{\epsilon_b}\epsilon'_b & \epsilon_b\bar{\epsilon_s}\epsilon'_b & \epsilon_b\bar{\epsilon_b}\epsilon'_s & \epsilon_b\bar{\epsilon_b}\epsilon'_b \\ \bar{\epsilon_s}\epsilon_s\epsilon'_s & \bar{\epsilon_s}\epsilon_s\epsilon'_b & \bar{\epsilon_s}\epsilon_b\epsilon'_s & \bar{\epsilon_b}\epsilon_s\epsilon'_s & \bar{\epsilon_s}\epsilon_b\epsilon'_b & \bar{\epsilon_b}\epsilon_s\epsilon'_b & \bar{\epsilon_b}\epsilon_b\epsilon'_s & \bar{\epsilon_b}\epsilon_b\epsilon'_b \\ \epsilon_s\bar{\epsilon_s}\bar{\epsilon'_s} & \epsilon_s\bar{\epsilon_s}\bar{\epsilon'_b} & \epsilon_s\bar{\epsilon_b}\bar{\epsilon'_s} & \epsilon_b\bar{\epsilon_s}\bar{\epsilon'_s} & \epsilon_s\bar{\epsilon_b}\bar{\epsilon'_b} & \epsilon_b\bar{\epsilon_s}\bar{\epsilon'_b} & \epsilon_b\bar{\epsilon_b}\bar{\epsilon'_s} & \epsilon_b\bar{\epsilon_b}\bar{\epsilon'_b} \\ \bar{\epsilon_s}\epsilon_s\bar{\epsilon'_s} & \bar{\epsilon_s}\epsilon_s\bar{\epsilon'_b} & \bar{\epsilon_s}\epsilon_b\bar{\epsilon'_s} & \bar{\epsilon_b}\epsilon_s\bar{\epsilon'_s} & \bar{\epsilon_s}\epsilon_b\bar{\epsilon'_b} & \bar{\epsilon_b}\epsilon_s\bar{\epsilon'_b} & \bar{\epsilon_b}\epsilon_b\bar{\epsilon'_s} & \bar{\epsilon_b}\epsilon_b\bar{\epsilon'_b} \\ \bar{\epsilon_s}\bar{\epsilon_s}\epsilon'_s & \bar{\epsilon_s}\bar{\epsilon_s}\epsilon'_b & \bar{\epsilon_s}\bar{\epsilon_b}\epsilon'_s & \bar{\epsilon_b}\bar{\epsilon_s}\epsilon'_s & \bar{\epsilon_s}\bar{\epsilon_b}\epsilon'_b & \bar{\epsilon_b}\bar{\epsilon_s}\epsilon'_b & \bar{\epsilon_b}\bar{\epsilon_b}\epsilon'_s & \bar{\epsilon_b}\bar{\epsilon_b}\epsilon'_b \\ \bar{\epsilon_s}\bar{\epsilon_s}\bar{\epsilon'_s} & \bar{\epsilon_s}\bar{\epsilon_s}\bar{\epsilon'_b} & \bar{\epsilon_s}\bar{\epsilon_b}\bar{\epsilon'_s} & \bar{\epsilon_b}\bar{\epsilon_s}\bar{\epsilon'_s} & \bar{\epsilon_s}\bar{\epsilon_b}\bar{\epsilon'_b} & \bar{\epsilon_b}\bar{\epsilon_s}\bar{\epsilon'_b} & \bar{\epsilon_b}\bar{\epsilon_b}\bar{\epsilon'_s} & \bar{\epsilon_b}\bar{\epsilon_b}\bar{\epsilon'_b} \end{pmatrix} \begin{pmatrix} n^*_{\gamma\gamma\gamma} \\ n^*_{\gamma\gamma j} \\ n^*_{\gamma j\gamma} \\ n^*_{j\gamma\gamma} \\ n^*_{\gamma jj} \\ n^*_{j\gamma j} \\ n^*_{jj\gamma} \\ n^*_{jjj} \end{pmatrix} \,,$$

where the

$$\boldsymbol{n} = \begin{pmatrix} n_{ppp} \\ n_{ppf} \\ n_{pfp} \\ n_{fpp} \\ n_{pff} \\ n_{fpf} \\ n_{ffp} \\ n_{fff} \end{pmatrix}$$

denotes a vector of observed events (p = passing, f = failing the photon selection) and the

$$\boldsymbol{n}^* = \begin{pmatrix} n^*_{\gamma\gamma\gamma} \\ n^*_{\gamma\gamma j} \\ n^*_{\gamma j\gamma} \\ n^*_{j\gamma\gamma} \\ n^*_{\gamma jj} \\ n^*_{j\gamma j} \\ n^*_{jj\gamma} \\ n^*_{jjj} \end{pmatrix}$$

denotes produced events. The $\boldsymbol{E}$ $(E_{ij},\ i, j = 1, \cdots, 8)$ is an 8×8 efficiency matrix, where the signal and background efficiencies $(\epsilon_s,\ \epsilon_b)$ are the probability of a photon and jet to pass the photon selection, and

$$\bar{\epsilon_s} \equiv 1 - \epsilon_s \,, \qquad \bar{\epsilon_b} \equiv 1 - \epsilon_b \,.$$

For calculating these probabilities, we choose a certain sub-set of selection cuts, referred to as the base cuts in what follows, to define the denominator objects. Furthermore, we introduce looser base-cuts only for the 3rd objects in order to improve the statistical power of our fake-background estimation, whichs correspond to the ϵ'_s and ϵ'_b in the efficiency matrix. The E_T dependence of the ϵ_s or ϵ'_s is neglected, while we take into account of it for the ϵ_b or ϵ'_b.

1. Rate of jets faking photons

We estimate the rate at which a jet originating from a quark or a gluon fakes an isolated photon in the central calorimeter to apply it as the ϵ_b or ϵ'_b in the efficiency matrix. We call any photon that is due to the decay of a meson

(e.g. $\pi^0/\eta^0 \to 2\gamma$) as "fake photons", whereas prompt photons via direct production or radiated off a quark make up the "true photon" signal.

Our analysis starts by measuring the raw jet-to-photon fake rate, which is simply the fraction of jets passing our selection cuts, for isolated jets found in a sample of jet-triggered events. The "raw" means that the selected photon candidates are a mixture of mis-identified hadronic quark/gluon showers and prompt photons. The raw fake-rate thus can be expressed by

$$P_{\rm raw} = \frac{N_\gamma^{\rm cand}}{N_j} = \frac{N_\gamma^{\rm true} + N_{j\to\gamma}}{N_j}$$

and it represents an upper limit on the actual fake-rate since it is contaminated by true photons $N_\gamma^{\rm true}$. The jet-triggerd datasets have a 9.7 fb^{-1} of integrated luminosity. We filter these QCD events by requiring that the ΔR separation between every pair of jets is at least 0.4, where $\Delta R = \sqrt{(\Delta\eta)^2 + (\Delta\phi)^2}$ is the radius in the η-ϕ space. The jets are further sub-divided into three groups from the highest to the lowest jet E_T. They are the 1st jet, 2nd jet, and "3 or more jets". We choose the "3 or more jets" in order to avoid possible biases by the jet triggers especially on the E_T, and it is referred to as the probe jets. The probe jets are required to satisfy $E_T > 15$ GeV and $|\eta| < 1.1$ to be considered for the raw fake-rate measurement. Having determined the QCD jet sample, we search in each event for the closest matching EM object to the selected jet. If the separation is $\Delta R < 0.4$, we accept the EM object as a candidate for faking a photon. We then require the base cuts to pick up the denominator objects. Finally we apply all the photon selection cuts to the matched EM objects to determine the number that would be accepted as central photons.

The jet samples used to measured the raw fake-rate contain "true" photons from direct production or bremsstrahlung radiation. The true photons have a high probability to pass the photon selection and thus increase the measured fake rate. A correction factor,

$$F_{\rm QCD} = \frac{N_{j\to\gamma}}{N_\gamma^{\rm cand}} = \frac{N_{j\to\gamma}}{N_\gamma^{\rm true} + N_{j\to\gamma}} \,,$$

which estimates the fraction of actual jets that are in our fake-rate sample, is applied to the raw fake-rate to correct for prompt-photon contamination and to obtain the "true" fake-rate $P_{\rm true}$ that is applied as the ϵ_b or ϵ_b' in the efficiency matrix. Correcting the raw fake-rate for prompt-photon contamination must be accomplished by statistical methods because the particle-by-particle identification is not possible. We use distributions on the plane of the isolation vs. χ^2-matching of the shower-profile to determine the $F_{\rm QCD}$ by assuming no correlation between the isolation energy and χ^2 for background events. Signal events congregate in the low isolation and good χ^2-matching region, while background events have large isolation energy due to hadronic activity.

The "true" fake rate for the QCD sample is obtained by

$$P_{\rm true} = \frac{N_{j\to\gamma}}{N_j} = \frac{N_\gamma^{\rm cand}}{N_j} \times \frac{N_{j\to\gamma}}{N_\gamma^{\rm cand}} = P_{\rm raw} \times F_{\rm QCD} \,,$$

which is shown in Fig. 4.

As a measure of the systematic errors we perform separate analyses and compare the fake rates for jet datasets with different trigger E_T thresholds. The variation is found to be approximately 5–15%.

2. Photon efficiency

We estimate the probability of a photon to pass the selection cuts to use it as the ϵ_s in the efficiency matrix. Because a pure sample of photons in the detector data is unavailable, the photon efficiency is estimated using efficiencies for electrons by assuming that electrons and photons behave similarly in the detector. Here we deal with the photon efficiency itself just for obtaining the efficiency matrix, rather than discussing the scale factors to MC efficiencies.

The high-p_T electron trigger is used to collect data from all the available datasets. The corresponding integrated luminosity is 9.6 fb^{-1}.

The process $Z \to ee$ is selected to define a pure sample of electrons. All $Z \to ee$ events are the central-central data. Each event is required to have an electron passing all the cuts, referred to as the tight cuts, and another passing the base cuts. We then look at their invariant mass distributions. The signal is assumed to take the form of a double-Gaussian distribution, while the background is taken to be the 3rd-degree polynomial. By fitting the

sum of these two functions to data, we fix the parameters of the Gaussian functions. The number of signal events is then estimated by integrating the Gaussian functions. After the number of events passing the cuts is calculated, the efficiency for these events can be determined.

In the case of two central electrons, the analysis creates a statistical bias because of the initial requirement of at least one tight electron in the central detector. As one tight central electron has already been required, the probability that the second central electron will pass the tight cuts is lower due to the two possible combinations of the tight and the base-cut pair. To reconcile this bias, the central-central efficiency equation must be modified. The equation used is

$$\epsilon = \frac{N_{TT} + N_{TT}}{N_{TB} + N_{TT}} ,$$

where the N_{TT} is the number of events with both legs passing all the tight cuts and the N_{TB} is the number of events with a tight leg and another leg passing at least the base cuts.

3. Calculation of fake event

The observed numbers of events $\boldsymbol{n}$ are related to the objects passing or failing the selection cuts. The jet objects with $E_T > 15$ GeV and $|\eta| < 1.1$ are considered in the photon sample explained in II. They must have a matched EM object passing the base cuts. If there are more than 3 such objects in a given event, we pick up the 3 objects from the highest E_T. We then examine whether these EM objects pass the photon selection or not. The n_{ppp} is the number of observed events which have 3 denominator objects passing the standard photon cut, the n_{ppf} is the number of observed events which have 2 objects passing standard photon cut and 1 object failing, and the same can be said for others.

The efficiency matrix $\boldsymbol{E}$ includes the ϵ_b or ϵ'_b which is the E_T dependent probability of a jet faking a photon. We take this event-by-event variation of the efficiency matrix by performing the matrix inversion for each event i, namely,

$$\boldsymbol{n}^* = \sum_i^{\text{events}} \boldsymbol{E}_i^{-1} \boldsymbol{e}_i ,$$

where the $\boldsymbol{e}_i$ is the basic vector of the pass-fail representation. For example, if a given event is classified as ppf, then

$$\boldsymbol{e}_i = \begin{pmatrix} 0 \\ 1 \\ 0 \\ 0 \\ 0 \\ 0 \\ 0 \end{pmatrix} ,$$

and so on.

The number of the QCD contribution is estimated by the following equation,

$$\begin{aligned} n^{3\gamma}_{\text{fake}} &= \epsilon_s^2\epsilon'_b \times n^*_{\gamma\gamma j} + \epsilon_s\epsilon_b\epsilon'_s \times n^*_{\gamma j\gamma} + \epsilon_b\epsilon_s\epsilon'_s \times n^*_{j\gamma\gamma} + \epsilon_s\epsilon_b\epsilon'_b \times n^*_{\gamma jj} \\ &+ \epsilon_b\epsilon_s\epsilon'_b \times n^*_{j\gamma j} + \epsilon_b\epsilon_b\epsilon'_s \times n^*_{jj\gamma} + \epsilon_b\epsilon_b\epsilon'_b \times n^*_{jjj} . \end{aligned}$$

and is found to be

$$n^{3\gamma}_{\text{fake}} = 2.99 \pm 0.23(\text{stat}) .$$

4. Systematic uncertainties

The systematic uncertainty on the number of fake events includes the uncertainties originating from the photon efficiency and the jet-to-photon fake rate. We take an uncertainty of 2.7% for the photon efficiency per photon. The contribution of this input uncertainty to the output number of fake events after applying our background-estimation method is found to be 0.2%. As the uncertainties of the input fake rates, we use the uncertainties shown in Fig. 4.

The plot shows the statistical and systematic uncertainties separately but the combined uncertainties of these fake rates are considered to be the source of the systematic uncertainty here. We find that it results in the uncertainty of 19% of the estimated number of fake-backgrounds.

We consider another source of the systematic uncertainty which is related to the sample dependence of the fake rates. The probability of a jet faking a photon depends on the fragmentation process of the quark or gluon that the jet is originating from. For example, the fragmentation producing a single neutral pion should have higher probabilities than the general cases. Then the fragmentation is basically different between quarks and gluons, which means that the fake rates are sensitive to the composition of quarks and gluons in the sample. We measure the fake rates in the gneric jet samples, while we apply them to events containing 3 objects of different combination of types such as $\{\gamma, j, j\}$, $\{j, \gamma, j\}$, $\{j, j, j\}$, and so on. The quark-gluon compositions could be largely different among them which would lead to errors of the estimated number of fake backgrounds.

In order to take this effect into account of, we take a conservative approach rather than evaluating details such as the quark-gluon composition of the samples, which in fact turns out sufficient for our analysis. We assume that our fake rates obtained from the generic samples correspond to the 50%-50% mixture of quarks and gluons. We may say that this is equivalent to, from the Bayesian viewpoint, assuming that we do not have any information regarding the composition. Furthermore, we assume that the fake rates for gluon jets and quark jets differ by as much as 50%. From these, the fake rates are controlled by a single parameter, the quark fraction in the sample, f_q, that is

$$\epsilon_b^* = \epsilon_b \cdot (f_q + 0.5) \,,$$

where the ϵ_b^* represents the unknown true fake-rate properly reflecting the quark-gluon composition of a given sub-sample of the photon events. We then generate f_q values uniformly in the range between 0 and 1, and repeat the calculation of the number of expected fake-photon backgrounds. In doing this, we use different f_q values for each of the type-combination, $\{j, j, j\}$, $\{\gamma, j, j\}$, $\{j, \gamma, j\}$, and so on. By this, we introduce the sample dependence of the fake rates, and at the same time, the correlation among the efficiency matrix elements is embedded in the evaluation. For example, the $\{j, j, j\}$ contributes to the $\{p, p, p\}$ through $E_{18} = \epsilon_b^* \epsilon_b^* \epsilon_b^{*'}$ and $\{p, p, f\}$ through $E_{28} = \epsilon_b^* \epsilon_b^* (1 - \epsilon_b^{*'})$, thus the E_{18} and E_{28} are correlated.

We generate 1000 trials and look at the variation of the estimated number of fake-photon backgrounds. The level of the variation is found to be 37%.

Adding all the systematic uncertainties in quadrature, the total systematic uncertainty is estimated to be 41%. As a summary, the fake-photon background we quote is

$$n_{\rm fake}^{3\gamma} = 3.0 \pm 0.2({\rm stat}) \pm 1.2({\rm syst}) \,.$$

B. Direct triphoton background

1. *Monte Carlo data*

We estimate the DTP background by using MC data based on the `MadGraph/MadEvent` (version 4) + `PYTHIA` parton-shower event generation. The `MadGraph/MadEvent` provides exact treetments of tree-level matrix elements for the DTP events. The number of jets allowed in one event at the `MadGraph/MadEvent` generation is 0–2. The 0-jet event corresponds to the LO tree-level process

$$q\bar{q} \to 3\gamma \,,$$

and the 1-jet event is the NLO tree-level processes

$$q\bar{q} \to (3\gamma) g \,, \qquad qg \to (3\gamma) q \,, \qquad \bar{q} g \to (3\gamma) \bar{q} \,,$$

then the 2-jet event consists of the NNLO tree-level processes

$$q\bar{q} \to (3\gamma) gg \,, \qquad qg \to (3\gamma) qg \,, \qquad \bar{q} g \to (3\gamma) \bar{q} g \,, \qquad gg \to (3\gamma) q\bar{q} \,.$$

We perform the so-called MLM matching between the matrix-element calculation and parton showering in order to remove double counting regarding the jet production. The parameter in the `MadGraph/MadEvent` to control the matching is named `xqcut` and we set `xqcut`$= 5$ to realize smooth distributions of the differential jet rate.

The number of generated events is about 2.6 M events (correponding to about 19 ab^{-1}) which are passed through our full detector-simulation. We pick up prompt photons by looking at the generator-level information, then apply the same photon selection as we do for the real data.

We then proceed with the estimation of the DTP incorporating the scale factors for the photon selection efficiency, and find the number of expected events to be

$$n^{3\gamma}_{\text{DTP}} = 6.906 \pm 0.058(\text{stat}) \,.$$

2. *Comparison with the* `MCFM`

We look at some aspects of the cross-section calculation by comparing the `MadGraph` with another matrix-element calculation tool called the `MCFM` (version 6.8). It provides a theoretical calculation of the full NLO cross section, including loop diagrams, which has been made available recently [13]. With a certain kinematical constraints on the parton-level final-states which is consistent with our analysis, the result of the cross-section calculations are compared. The LO cross-section by the `MadGraph/MadEvent` is 2.617 fb, and the same LO cross-section by the `MCFM` is 2.787 fb. The difference is 6.5%. The NLO cross-section without loop diagrams by the `MadGraph/MadEvent` is 4.911 fb, while the full NLO cross-section by the `MCFM` is found to be 4.667 fb. One thing to be noted is that the `MadGraph/MadEvent` predicts rather large contributions from 2-jet events. The overall difference between the `MadGraph/MadEvent` and the `MCFM` is as much as

$$\frac{4.667}{6.840} = 0.682 \qquad \text{or} \qquad 32\% \text{ difference} \,.$$

3. *Systematic uncertainties*

The systematic uncertainty of the number of DTP events originating from the normalization is estimated to be 7.2% by changing the renormalization scale in the range between $0.5M_{3\gamma}$ and $2M_{3\gamma}$. We also quote 32% related to the normalization systematics by conservativly taking the difference of the cross sections between the `MadGraph/MadEvent` and the `MCFM` calculations. We take 1.1% for the matching uncertainty which is estimated by changing the `xqcut` parameter by ± 1. For the systematic uncertainties from the PDF and ISR/FSR, we follow the same procedure used for the signal efficiency. The systematic uncertainty from the PDF is found to be 1.2%, and the uncertainty from the ISR/FSR is 5.7%. The uncertainty from the photon efficiencies is $3 \times 2.7\% = 8.1\%$. Finally, the uncertainty due to the luminosity is 6% with major contributions from the uncertainties on the efficiency of the luminosity counter, the detector simulation, and the event generator.

Adding these uncertainties in quadrature, we obtain the total systematic uncertainty of 35%. The estimated number of DTP events is then given by

$$n^{3\gamma}_{\text{DTP}} = 6.9 \pm 0.1(\text{stat}) \pm 2.4(\text{syst}) \,.$$

C. Electroweak processes

We investigate the contributions from electroweak processes using the MC data with calibrating them by real data as much as possible. We considered

$$Z(\to ee)\gamma \,, \qquad W(\to e\nu)\gamma \,, \qquad Z(\to \tau\tau)\gamma \,, \qquad W(\to \tau\nu)\gamma \,,$$

and the expected total number of events is estimated to be

$$n^{3\gamma}_{\text{EWK}} = 0.45 \pm 0.06(\text{stat}) \pm 0.32(\text{syst}) \,.$$

D. Summary of background estimation

The total background to the $3\gamma + X$ final state is estimated by the sum of $n^{3\gamma}_{\text{fake}}$, $n^{3\gamma}_{\text{DTP}}$, and $n^{3\gamma}_{\text{EWK}}$. Table I summarizes the systematic errors and Table II shows the estimated total background events with statistical and systematic errors. The number of events found in the data is also included in the table.

V. OPTIMIZATION

A. Optimization and expected limits

Now that the background estimation methods are determined and the signal efficiency is available, along with their uncertainties, an optimization procedure can be employed.

We choose to optimize the $E_T^{\gamma_1} + E_T^{\gamma_2}$ cut. Let us recall that the signal event has four photons, and two jets or a lepton from a W boson. Each object is quite energetic carrying on average 10–20 GeV of energy in the transverse plane. Thus the h_f signal has a large $E_T^{\gamma_1} + E_T^{\gamma_2}$ compared to the SM backgrounds which are dominated by the fake and DTP backgrounds.

As a measure of our search sensitivity, we use 95% C.L. expected cross section limits, under the no-signal assumption, then find an optimal cut. We use the Bayesian limit calculation to obtain the limits, taking into account of the signal efficiency, the predicted number of background events, the luminosity, and their systematic uncertainties as well as the theoretical uncertainty of the cross section. The electroweak backgrounds are not included in this optimization since their contributions are small.

The systematic uncertainty of the signal efficiency is 8.9% as discussed in III B. We take 20% as the theoretical uncertainty on the prediction of production cross section for signals [14]. The systematic unertainty of the luminosity is taken to be 6%. These systematic uncertainties on the number of signal events are alreay included in Table I. The systematic uncertainty of the backgrounds is determined from our understanding of fake events and DTP events, as described in IV.

The predicted number of background events and the efficiency are a function of cut choice, so the expected cross section limit is also a function of cut value. For each combination of the h_f and $H^{\pm}$ masses, the minimum expected cross section limit defines our optimal cut. The mass exclusion is given by the region where the theoretical cross section is above the 95% C.L. cross section limit. We choose $E_T^{\gamma_1} + E_T^{\gamma_2} > 90$ GeV as this cut reasonably maximizes and stabilizes the mass limits. Figure 5 shows the $E_T^{\gamma_1} + E_T^{\gamma_2}$ distribution with the final signal region indicated. A cumulative distribution of the $E_T^{\gamma_1} + E_T^{\gamma_2}$, that is, the integration of the $E_T^{\gamma_1} + E_T^{\gamma_2}$ distribution toward the high $E_T^{\gamma_1} + E_T^{\gamma_2}$ region as a function of $E_T^{\gamma_1} + E_T^{\gamma_2}$, is shown in Fig. 6. Here we are comparing the background distribution and the expected signal for an example mass of $h_f = 75$ GeV/c^2 and mass of $H^{\pm} = 120$ GeV/c^2. The plot also includes the total error for the expected background estimation. When the background contributions are added, 100% correlation is assumed for the same error sources for a given bin.

B. Final search region

With the final cut of $E_T^{\gamma_1} + E_T^{\gamma_2} > 90$ GeV, we predict 2.96 ± 0.94 background events with 0.32 ± 0.16 of fake events, 2.60 ± 0.93 of DTP events, and 0.04 ± 0.03 of electroweak processes. Table III shows the expected number of background events and the number of events found in the data. Figures 7–11 show various distributions in the final 3γ events. Event displays for the 5 candidate events found in the data are shown in Figs. 12–16.

One may be curious about the staistical significance of the upward fluctuation of the observed data that we see, for example, in the bottom plot of Fig. 10. At the bin of $E_T^{\gamma_1} + E_T^{\gamma_2} + E_T^{\gamma_3} = 340$ GeV, we observe two events while the background expectation is 0.036 ± 0.014. The significance is derived from the so-called p value. The p-value calculation is performed in the framework of the prior-predictive method, i.e. the observed number of events is modeled by the Poisson statistics multiplied by the background prior with integrating nuisance parameters out. We use the truncated Gaussian as the background prior, then the probability density function (PDF) of the observed number of events is given by

$$\mathcal{P}(n|B, \Delta B) = \int_0^{+\infty} db \frac{e^{-b} b^n}{n!} \tilde{G}(b|B, \Delta B) \,, \tag{2}$$

where $\tilde{G}(b|B, \Delta B)$ represents a truncated Gaussian with the mean B and the sigma ΔB. When the observed number of events is given by n_0, we compute the p value with the test statistic n by

$$p = \sum_{n=n_0}^{+\infty} \mathcal{P}(n|B, \Delta B) \,. \tag{3}$$

Then, we use one-sided conversion of the p value to the sigma s:

$$p = 1 - \mathrm{Freq}(s) \,, \tag{4}$$

where the Freq(x) is the frequency function defined by

$$\mathrm{Freq}(x) \equiv \frac{1}{\sqrt{2\pi}} \int_{-\infty}^{x} dt\, e^{-\frac{t^2}{2}} \ . \tag{5}$$

By performing this exercise for the point in Fig. 10, we find the significance of 3.2σ. If we integrate the number of expected backgrounds from this bin to those in the higher region, we find the significance of 2.3σ, while it is 0.7σ if we integrate the number of expected backgrounds from the bin next to the 2nd highest observed event at 180 GeV.

VI. ANALYSIS CHECKS

Before going to the final result, we define some categories of events in which the signal events are minimized to confirm consistency between our background expectations and the observed data. We call it here the "control regions", although signal events could still contribute to the regions and they are not completely controlled.

The first type of events we consider are the sum of n_{ppf}, n_{pfp}, and n_{fpp} categories. What we have to do is just to extend the fake-background estimation already done for the n_{ppp} component to others. It provides a general check of our machinery, such as the matrix inversion, used to estimate the background. By repeating the fake and DTP background estimation for these components, we see that the predictions and the observed number of events are in good agreements.

We look at the region $E_T^{\gamma_1} + E_T^{\gamma_2} < 90$ GeV as another check of our background estimation. In order to minimize the signal contribution, we impose an additional cut

$$E_T^{\gamma_3} < 24 \text{ GeV}$$

on top of the $E_T^{\gamma_1} + E_T^{\gamma_2} < 90$ GeV cut. The counting result is shown in Table IV. Figures 17–22 show various distributions for $3\gamma + X$ events in this control region. We see reasonable agreements between our expectation and the data.

We vary the tightness of the selection for denominator objects to see how stable the fake-background estimation is. By doing so, the fake rates and photon efficiency also change, but the estimated fake-background should be consistent within the quoted uncertainties since the final selection is kept the same. Also, we compare the cases where we introduce the loose base-cuts or not. The fake-background estimations are stable within the quoted uncertainties.

Our nominal MC data are created by the `MadGraph/MadEvent` which does not include the loop diagrams. We check whether this fact significantly affects the predicted distributions by comparing $E_T^{\gamma_1} + E_T^{\gamma_2}$ between the `MadGraph/MadEvent` and the `MCFM` predictions, and both distributions are similar to each other.

As discussed in IV B 2, the `MadGraph/MadEvent` predicts rather large contributions from $3\gamma + 2j$ events. It would be thus interesting to see if there are any hints for it in the data, but it is inconclusive mainly due to low statistics of the real data.

VII. FINAL RESULTS

Figures 23 and 24 are examples of the expected and the observed cross-section limits at the 95% C.L. with $\pm 1\sigma$ and $\pm 2\sigma$ bands for a particular $H^{\pm}$ or h_f mass. The excluded mass regions are displayed on the m_{h_f}-$m_{H^{\pm}}$ plane in Fig. 25.

The excluded m_{h_f} values by the DØ analysis for $\tan\beta = 30$ is indicated in the version of Fig. 26 as two vertical lines corresponding to the two $H^{\pm}$-mass points they study. We added a shaded region between the two lines as it is naturally expected to be excluded. The left vertical line indicates that they reach a maximum sensitivity because the upper end is close to the kinematical limit. Therefore, the left side of this line would be also excluded by their analysis as our analysis does.

The effects of different $\tan\beta$ values are noticable when, especially, the m_{h_f} is close to the $m_{H^{\pm}}$, i.e. the kinematical limit. For example, the production cross-section would change by a factor of as much as $\simeq 100$ when $\tan\beta$ is changed from $\tan\beta = 3$ to $\tan\beta = 30$ for $(m_{h_f}, m_{H^{\pm}}) = (80, 100)$ GeV/c^2 [10]. The factor of 10 increase of the production cross-section would result in the m_{h_f} limit change of about 10 GeV/c^2 as we see, for example, from the $m_{H^{\pm}} = 120$ GeV/c^2 result in Fig. 23. In this kinematical region, the $\mathcal{B}(H^{\pm} \to h_f W^{\pm})$ becomes smaller due to smaller available phase-space and becomes comparable to the suppressed $H^{\pm}$ decays to fermions. The way to bring the sensitivity back is to make $\mathcal{B}(H^{\pm} \to h_f W^{\pm})$ larger by further suppressing the $H^{\pm}$ decays to fermions with larger $\tan\beta$ values. In other

kinematical regions, $\tan\beta$ does not affect the search sensitivity so much if $\tan\beta > 10$ because the coupling $\propto \sin\beta$ is already saturated and the $\mathcal{B}(H^{\pm}\to h_f W^{\pm})$ is always dominant. The corresponding excluded mass-regions are shown in Fig. 27, respectively. Figure 28 include the results from the DØ analysis as a reference.

VIII. CONCLUSIONS

We searched for the fermiophobic Higgs boson (h_f) in the two Higgs double model (type I) using the $3\gamma + X$ final state coming from the process

$$p\overline{p}\to h_f H^{\pm}\to h_f(h_f W^*)\to 4\gamma + X\ .$$

The number of background events was estimated to be 2.96 ± 0.94 for the integrated luminosity of 9.2 fb^{-1}, which was dominated by the contribution from direct triphoton events. The observed number of events was 5, which was consistent with the expected number of background events. The numbers of signal events were estimated for the m_{h_f} ranging from 10 to 105 GeV/c^2 and for $m_{H^{\pm}}$ from 30 to 300 GeV/c^2, which were then translated to the excluded mass region on the m_{h_f} vs. $m_{H^{\pm}}$ plane at the 95% confidence level.

TABLE I: Summary of systematic errors for the counting experiments.

$h_f H^\pm \to 3\gamma + X$	CDF Run II Preliminary: 9.2 fb^{-1}			
Sources	Uncertainty (%)			
	Signal	Fakes	DTP	EWK
Photon selection	8	1	8	8
PDF	1	—	1	—
ISR/FSR	2	—	6	—
Fake rates	—	23	—	—
q/g composition	—	37	—	—
Parton-shower matching	—	—	1	—
Cross section	20	—	33	—
EWK normalization	—	—	—	70
Luminosity	6	—	6	6
Total	23	43	35	72

TABLE II: Total background to the $3\gamma + X$ final state.

$h_f H^\pm \to 3\gamma + X$					CDF Run II Preliminary: 9.2 fb^{-1}
	Events ($E_T^{\gamma 1} + E_T^{\gamma 2} > 30$ GeV: control+signal regions)				
			(stat)		(syst)
Fake	3.0	±	0.2	±	1.2
Direct triphoton	6.9	±	0.1	±	2.4
Electroweak	0.4	±	0.1	±	0.3
Total	10.3	±	0.2	±	2.7
Data	10				

TABLE III: Background to the $3\gamma + X$ final state for the final selection requirement.

$h_f H^{\pm} \to 3\gamma + X$					CDF Run II Preliminary: 9.2 fb^{-1}
	Events ($E_T^{\gamma 1} + E_T^{\gamma 2} > 90$ GeV: signal region)				
			(stat)		(syst)
Fake	0.32	±	0.07	±	0.15
Direct triphoton	2.60	±	0.04	±	0.93
Electroweak	0.04	±	0.01	±	0.03
Total	2.96	±	0.08	±	0.94
Data	5				

TABLE IV: Events in the pilot regions and data.

$h_f H^{\pm} \to 3\gamma + X$					CDF Run II Preliminary: 9.2 fb^{-1}
	Events (control region)				
			(stat)		(syst)
Fake	2.56	±	0.16	±	1.05
Direct triphoton	3.74	±	0.04	±	1.31
Electroweak	0.32	±	0.05	±	0.22
Total	6.62	±	0.17	±	1.69
Data	5				

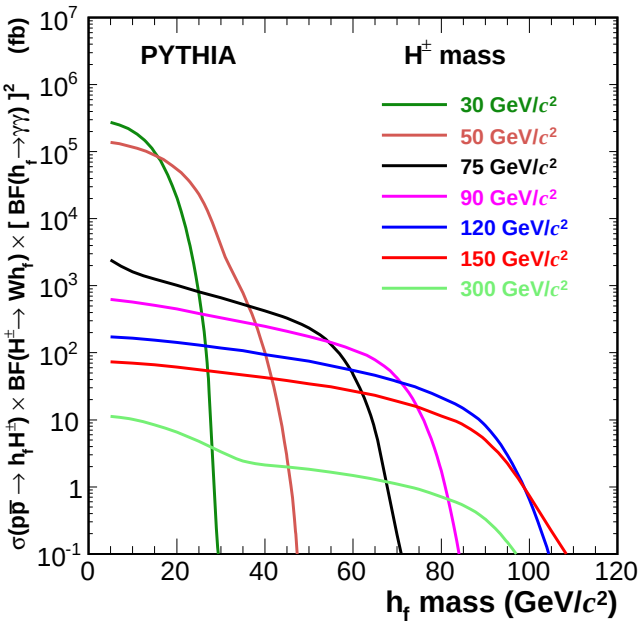

FIG. 1: Cross section for $p\bar{p} \to h_f H^{\pm} \to h_f h_f W \to \gamma\gamma\gamma\gamma + X$.

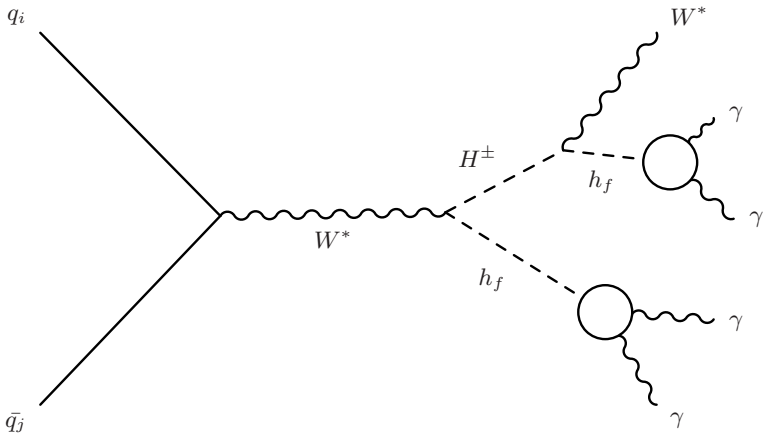

FIG. 2: A Feynman diagram for the fermiophobic higgs production and decay.

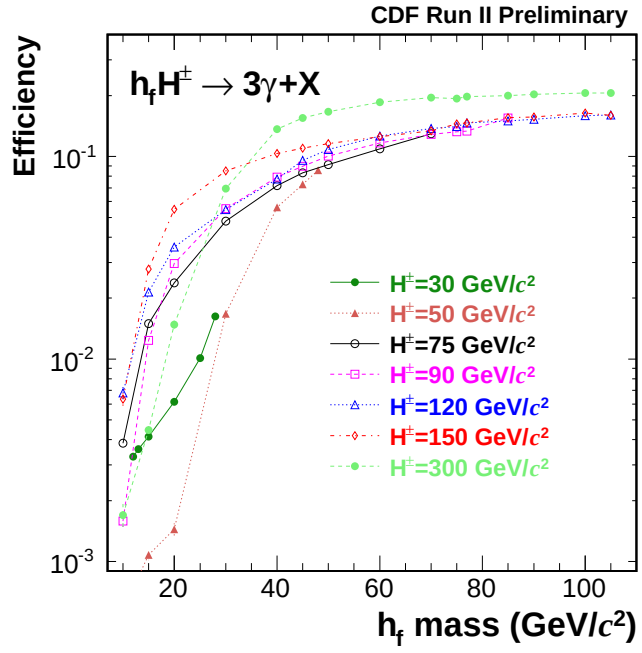

FIG. 3: Efficiencies of the h_f detection.

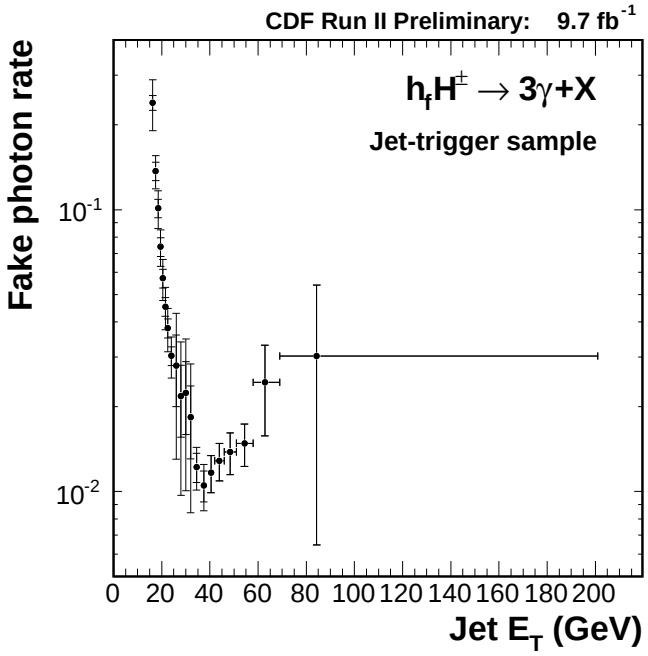

FIG. 4: True fake-rates ($P_{\rm true}$) with statistical errors (inner error-bars) and total errors (outer error-bars) for the combined jet datasets.

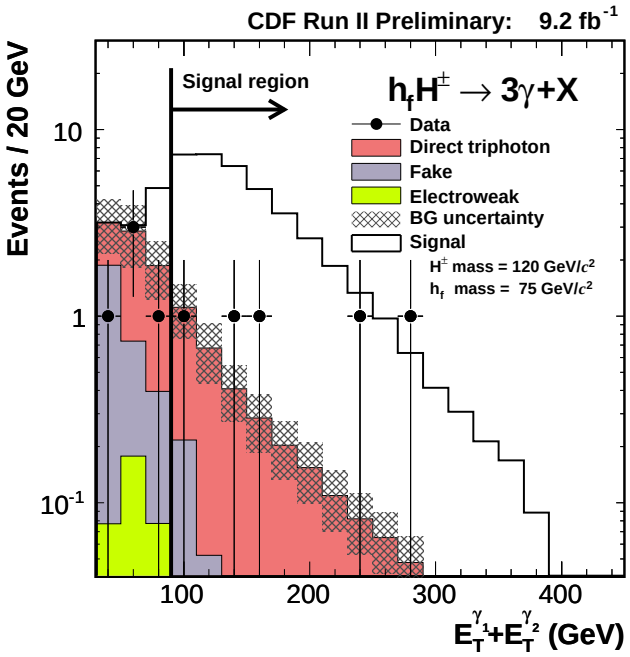

FIG. 5: Distribution of $E_T^{\gamma 1} + E_T^{\gamma 2}$ for the $3\gamma + X$ events expected from the SM backgrounds together with the expected signal events for $m_{h_f} = 75$ and $m_{H^\pm} = 120$ GeV/c^2.

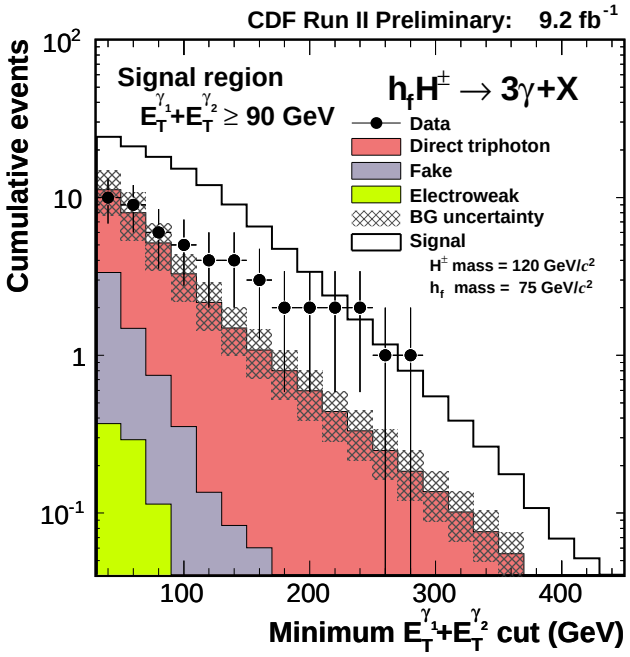

FIG. 6: Cumulative distribution of $E_T^{\gamma 1} + E_T^{\gamma 2}$ for the $3\gamma + X$ events expected from the SM backgrounds together with the expected signal events for $m_{h_f} = 75$ and $m_{H^\pm} = 120$ GeV/c^2.

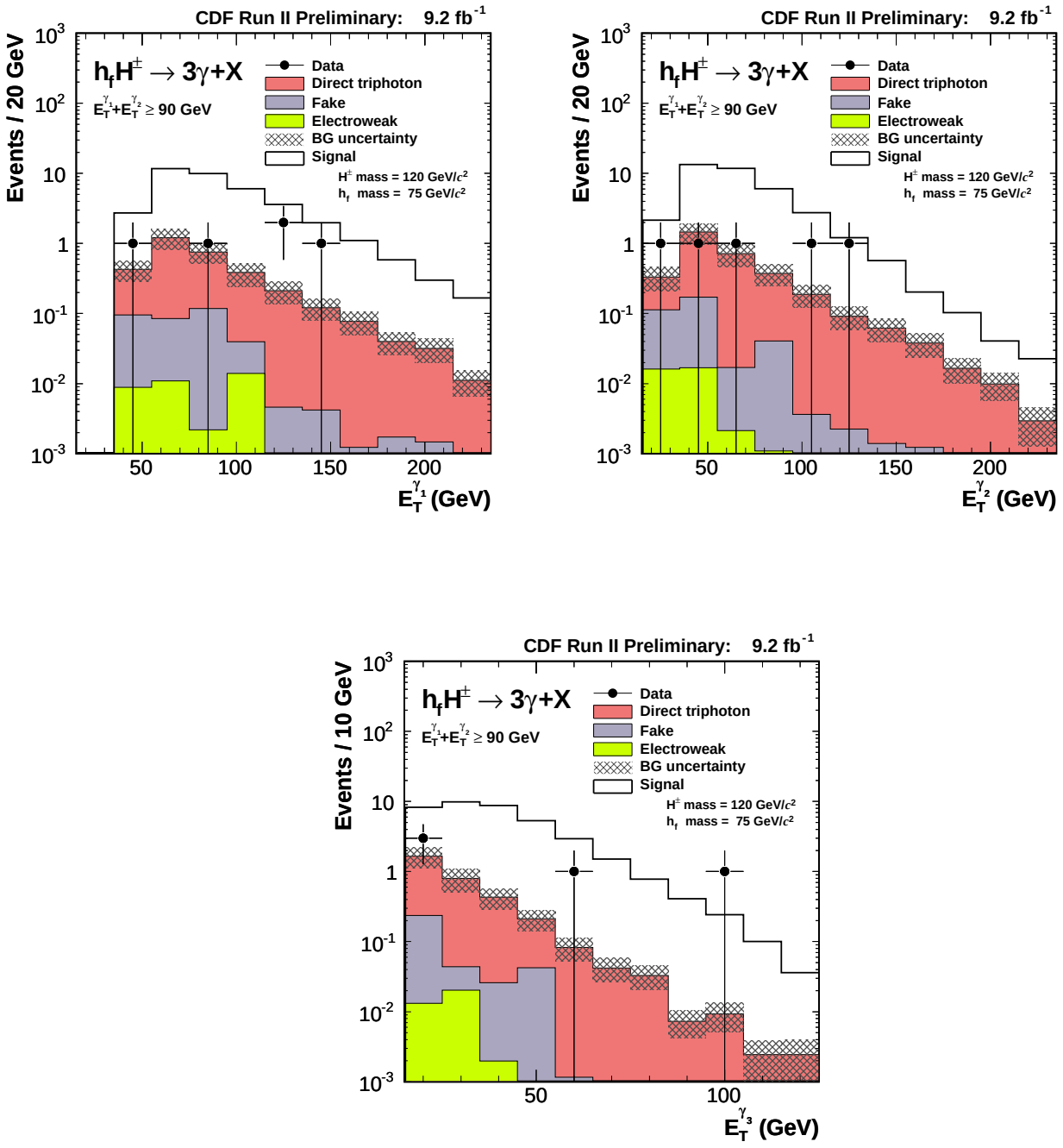

FIG. 7: Distributions of each E_T for the $3\gamma + X$ events with $E_T^{\gamma 1} + E_T^{\gamma 2} > 90$ GeV expected from the SM backgrounds and expected signal events for $m_{h_f} = 75$ and $m_{H^\pm} = 120$ GeV/c^2.

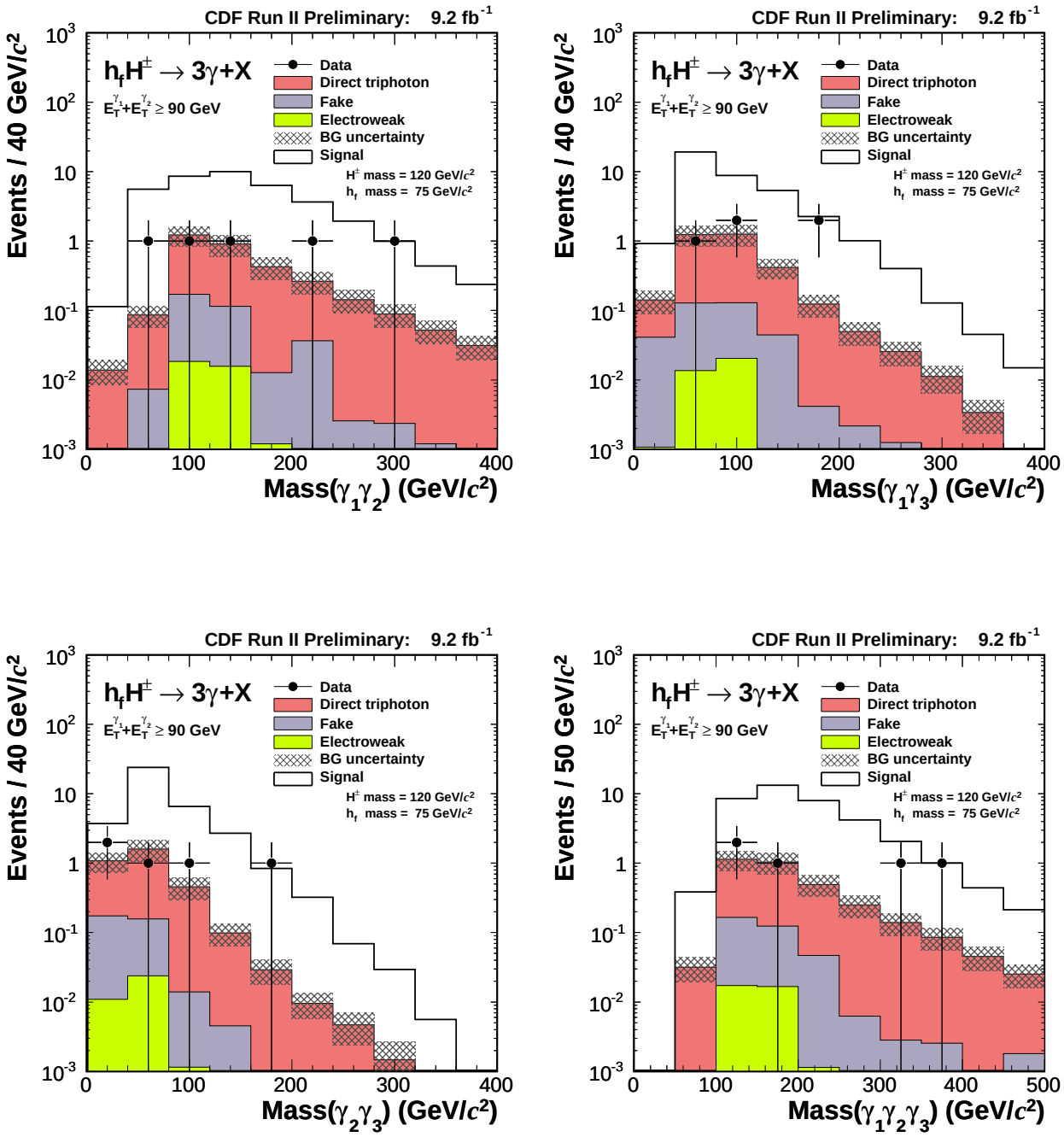

FIG. 8: Distributions of invariant mass of each pair of photons (the top two plots and bottom left plot) and three photons (the bottom right plot) for the $3\gamma + X$ events with $E_T^{\gamma 1} + E_T^{\gamma 2} > 90$ GeV expected from the SM backgrounds and expected signal events for $m_{h_f} = 75$ and $m_{H^\pm} = 120$ GeV/c^2.

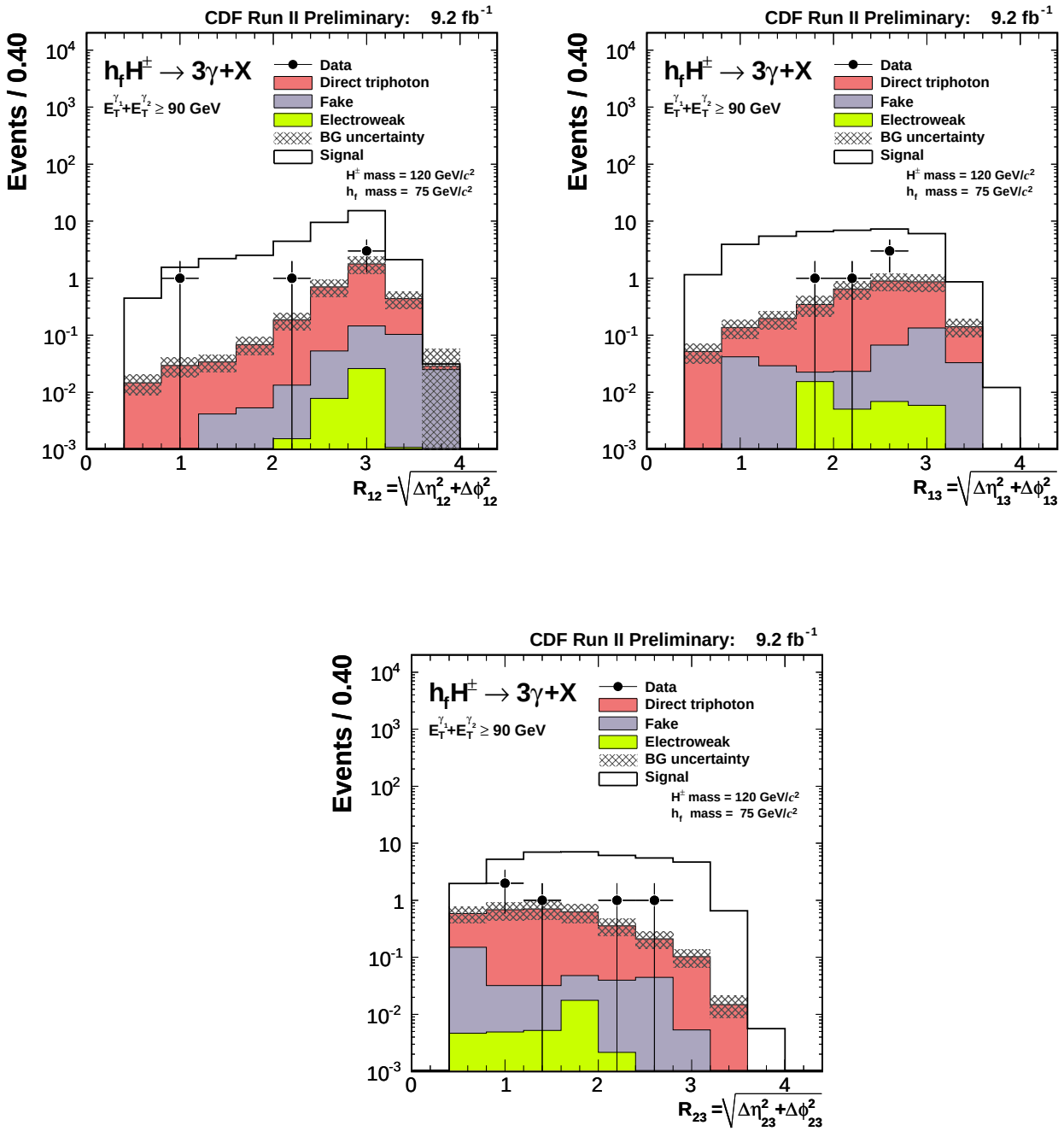

FIG. 9: Distributions of R (the distance in the η-ϕ plane between each pair of photons for the $3\gamma + X$ events with $E_T^{\gamma 1} + E_T^{\gamma 2} >$ 90 GeV expected from the SM backgrounds and expected signal events for $m_{h_f} = 75$ and $m_{H^{\pm}} = 120$ GeV/c^2.

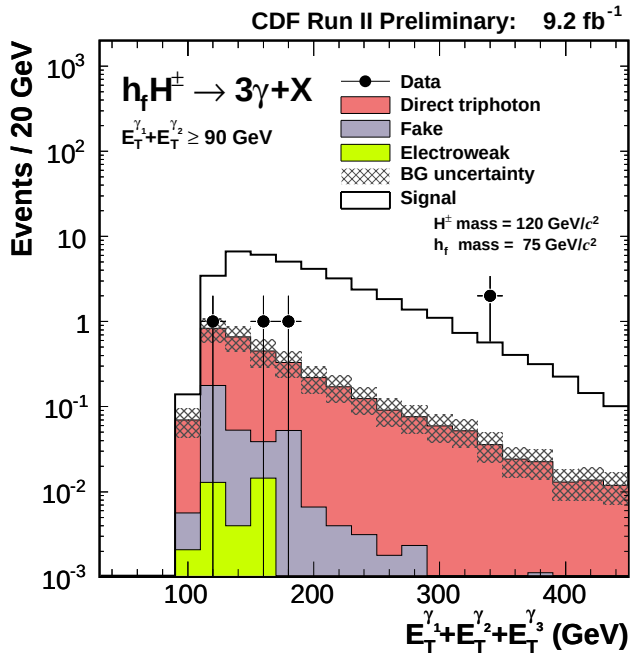

FIG. 10: Distributions of various sum of E_T for the $3\gamma+X$ events with $E_T^{\gamma 1} + E_T^{\gamma 2} > 90$ GeV expected from the SM backgrounds and expected signal events for $m_{h_f} = 75$ and $m_{H^\pm} = 120$ GeV/c^2.

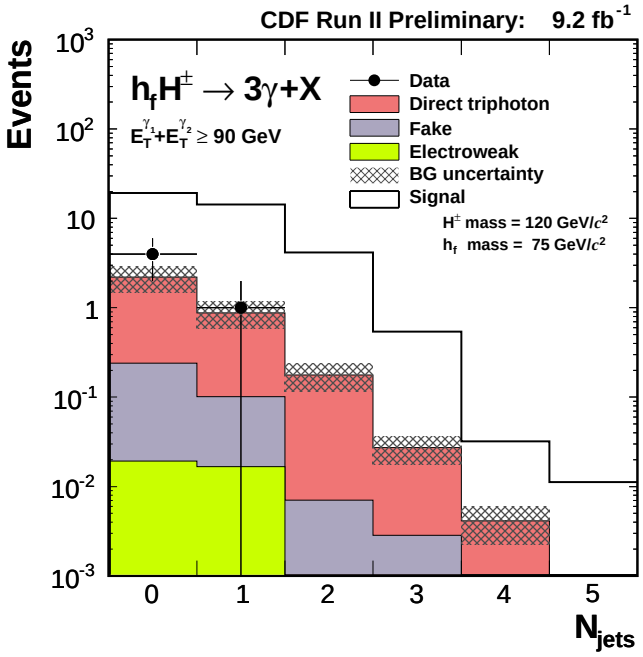

FIG. 11: The number of jets in the central region with $E_T > 10$ GeV for the $3\gamma+X$ events with $E_T^{\gamma 1} + E_T^{\gamma 2} > 90$ GeV expected from the SM backgrounds and expected signal events for $m_{h_f} = 75$ and $m_{H^\pm} = 120$ GeV/c^2.

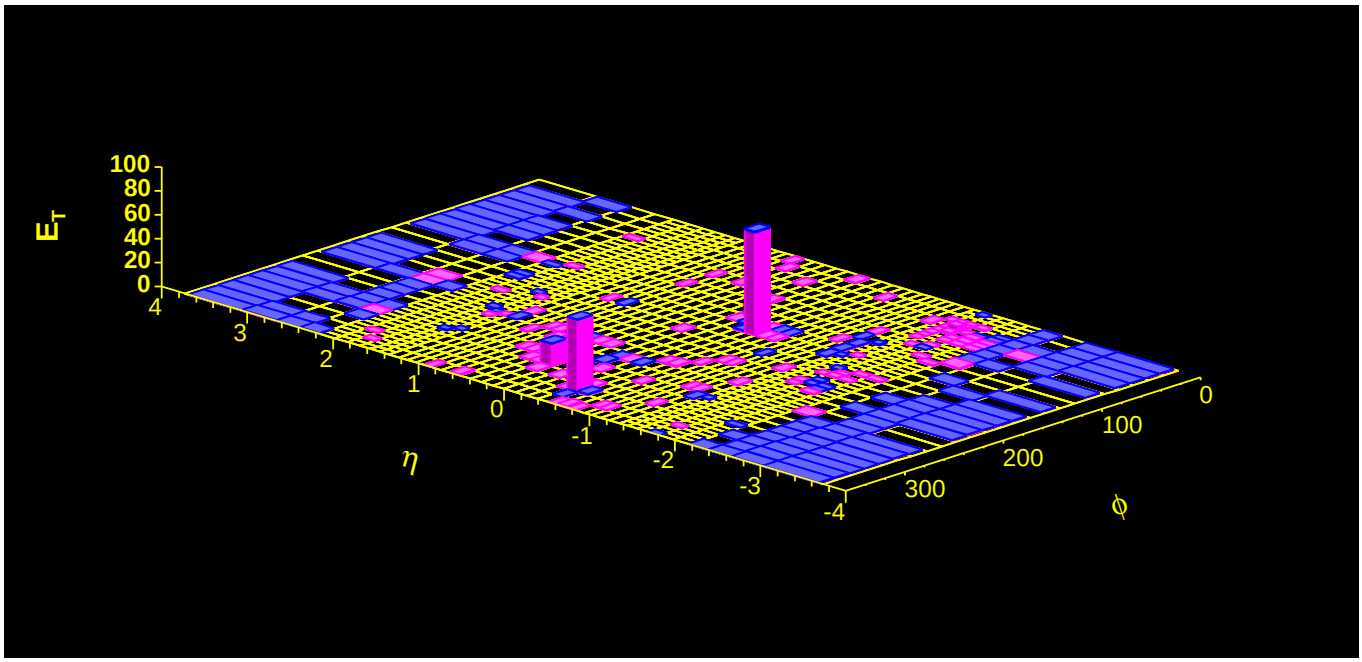

FIG. 12: Event display of a candidate event.

Run = 222357, Event = 8135145	
1st (E_T, η, ϕ)	= (82 GeV, −0.56, 2.53)
2nd (E_T, η, ϕ)	= (56 GeV, −0.60, 5.69)
3rd (E_T, η, ϕ)	= (19 GeV, +0.06, 5.22)
Corrected $\not\!\!E_T$	= 14 GeV
$\phi(\not\!\!E_T)$	= 2.63
(M_{12}, M_{23}, M_{31})	= (136, 27, 81) GeV/c^2
Extra jet $(E_T > 10$ GeV) (E_T, η, ϕ)	= (12 GeV, −1.80, 0.78)

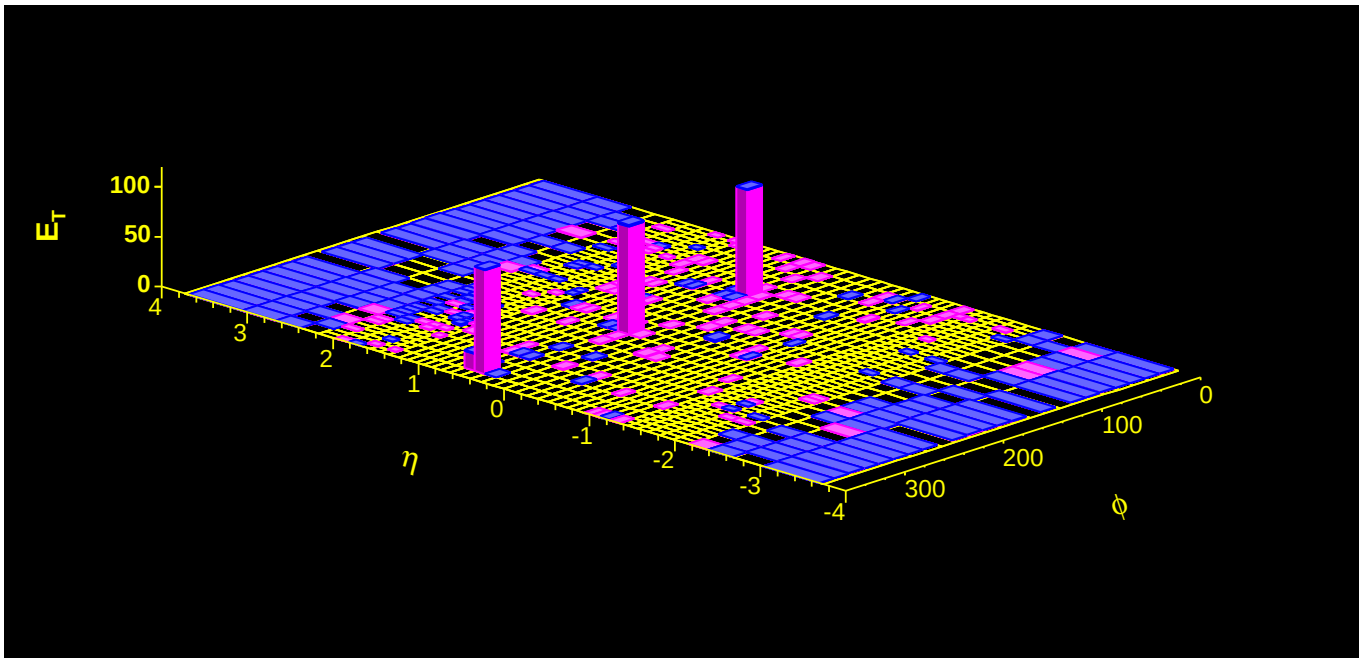

FIG. 13: Event display of a candidate event.

Run = 244996, Event = 6884022	
1st (E_T, η, ϕ)	= (117 GeV, +0.58, 5.87)
2nd (E_T, η, ϕ)	= (106 GeV, +0.40, 3.56)
3rd (E_T, η, ϕ)	= (100 GeV, +0.44, 1.53)
Corrected $\not\!\!E_T$	= 18 GeV
$\phi(\not\!\!E_T)$	= 5.12
(M_{12}, M_{23}, M_{31})	= (214, 181, 187) GeV/c^2

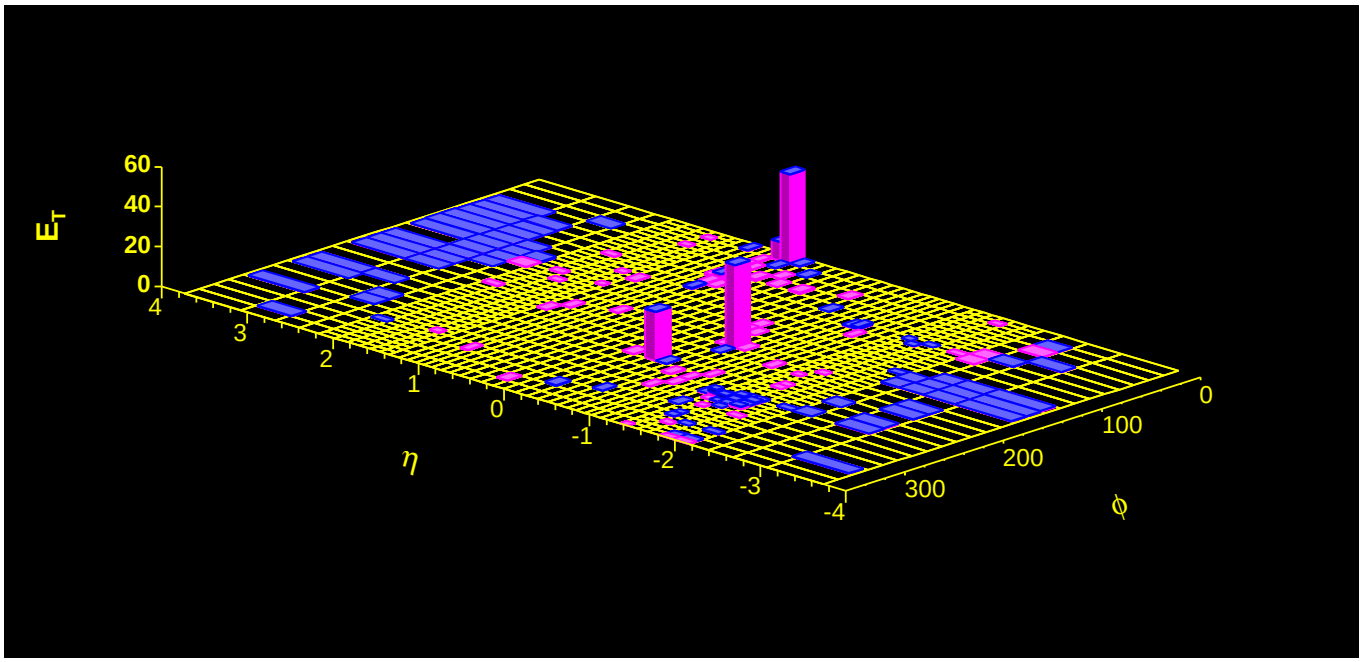

FIG. 14: Event display of a candidate event.

Run = 265489, Event = 11130875	
1st (E_T, η, ϕ)	= (54 GeV, +0.68, 0.19)
2nd (E_T, η, ϕ)	= (40 GeV, −0.59, 3.08)
3rd (E_T, η, ϕ)	= (24 GeV, −0.36, 4.02)
Corrected $\not\!\!E_T$	= 24 GeV
$\phi(\not\!\!E_T)$	= 0.70
(M_{12}, M_{23}, M_{31})	= (112, 29, 79) GeV/c^2
Extra jet $(E_T > 10$ GeV) (E_T, η, ϕ)	= (15 GeV, −1.55, 4.63)

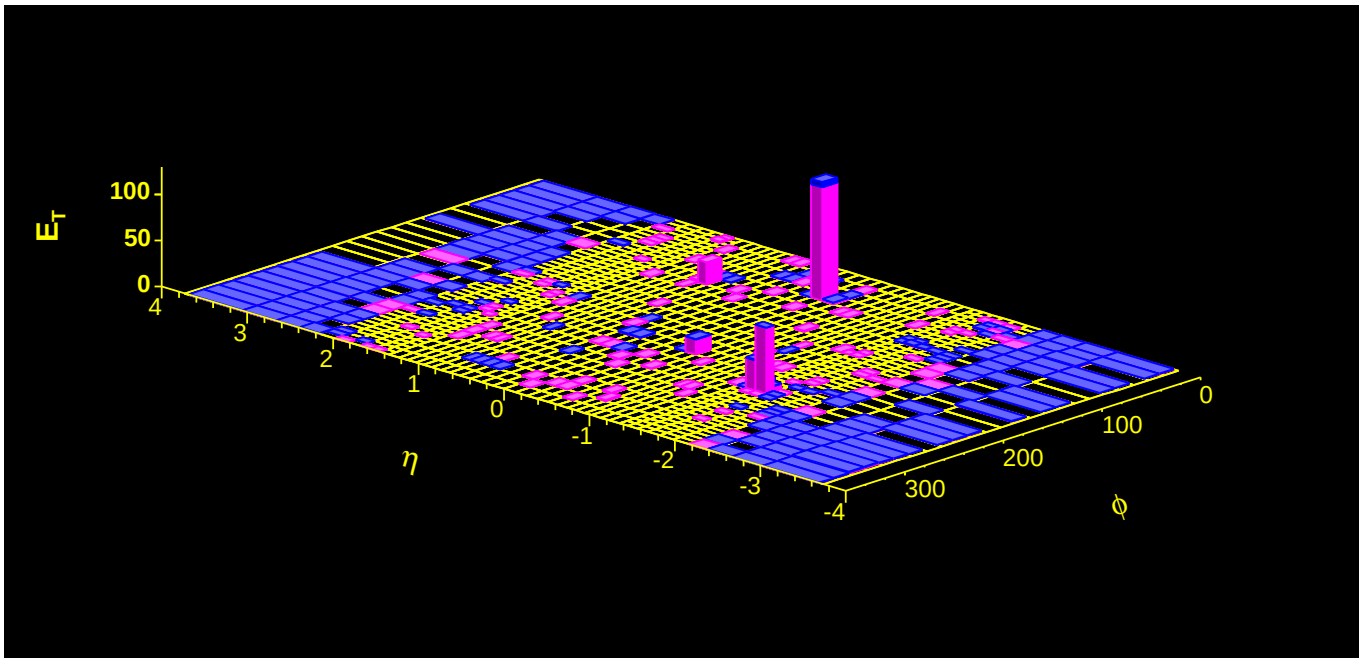

FIG. 15: Event display of a candidate event.

Run = 271004, Event = 5566848	
1st (E_T, η, ϕ)	= (129 GeV, $-0.09, 0.94$)
2nd (E_T, η, ϕ)	= (24 GeV, $+0.91, 1.33$)
3rd (E_T, η, ϕ)	= (17 GeV, $-0.28, 3.62$)
Corrected $\not\!\!E_T$	= 20 GeV
$\phi(\not\!\!E_T)$	= 4.48
(M_{12}, M_{23}, M_{31})	= $(63, 45, 91)$ GeV/c^2
Plug EM (E_T, η, ϕ)	= (136 GeV, $-1.40, 4.08$)
(M_{14}, M_{24}, M_{34})	= $(265, 64, 121)$ GeV/c^2
Low quality track (p_T, η, ϕ)	= (181 GeV/c, $+0.94, 1.63$)
Low quality track	29 COT hits (13 axial, 16 stereo), 3 segments.

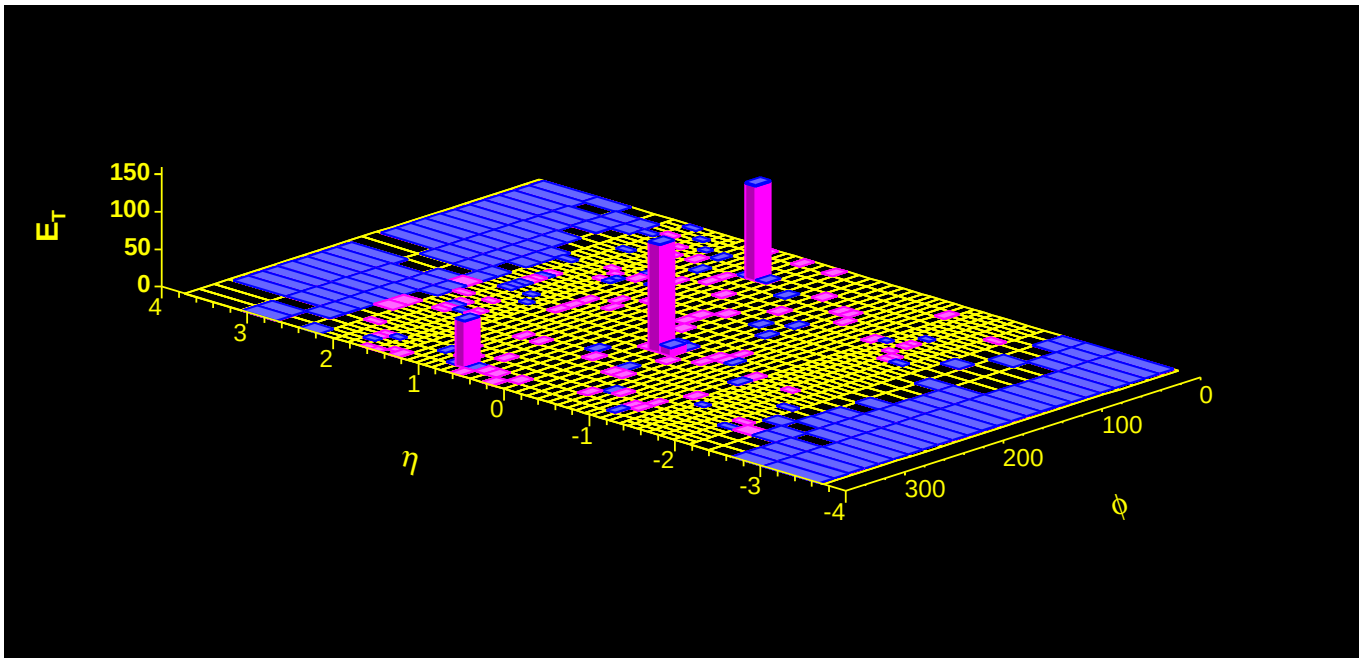

FIG. 16: Event display of a candidate event.

Run = 307408, Event = 2591643	
1st (E_T, η, ϕ)	= (152 GeV, −0.24, 3.69)
2nd (E_T, η, ϕ)	= (128 GeV, +0.56, 0.94)
3rd (E_T, η, ϕ)	= (63 GeV, +0.69, 5.88)
Corrected $\not\!\!E_T$	= 27 GeV
$\phi(\not\!\!E_T)$	= 3.77
(M_{12}, M_{23}, M_{31})	= (293, 108, 195) GeV/c^2

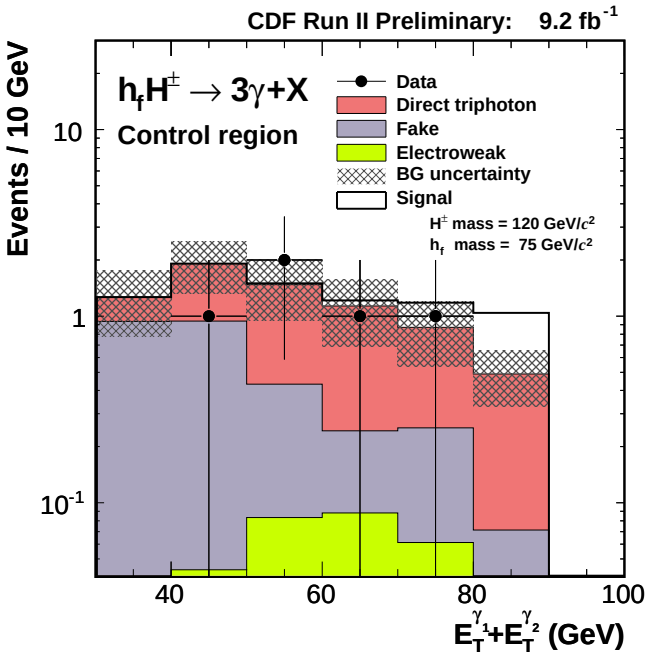

FIG. 17: Distribution of $E_T^{\gamma 1} + E_T^{\gamma 2}$ for the $3\gamma + X$ events with $E_T^{\gamma 1} + E_T^{\gamma 2} < 90$ GeV and $E_T^{\gamma 3} < 24$ GeV, expected from the SM backgrounds and expected signal events for $m_{h_f} = 75$ and $m_{H^\pm} = 120$ GeV/c^2.

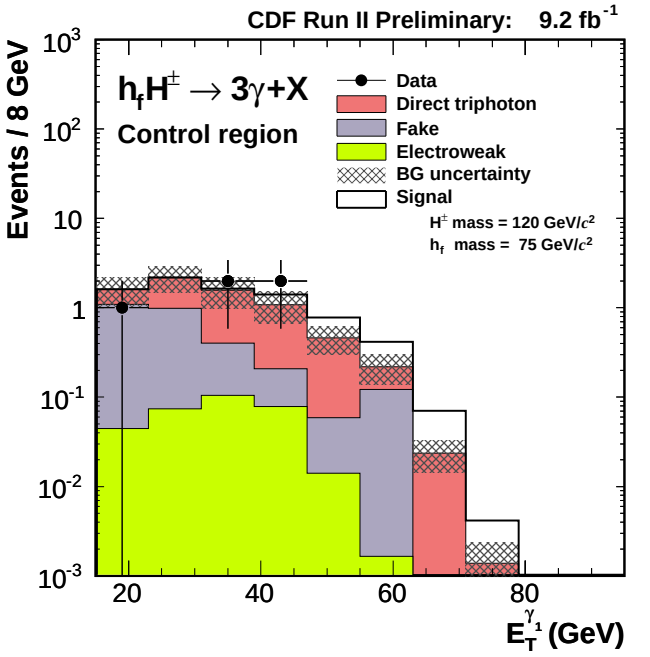

FIG. 18: Distributions of each E_T for the $3\gamma + X$ events with $E_T^{\gamma 1} + E_T^{\gamma 2} < 90$ GeV and $E_T^{\gamma 3} < 24$ GeV, expected from the SM backgrounds and expected signal events for $m_{h_f} = 75$ and $m_{H^\pm} = 120$ GeV/c^2.

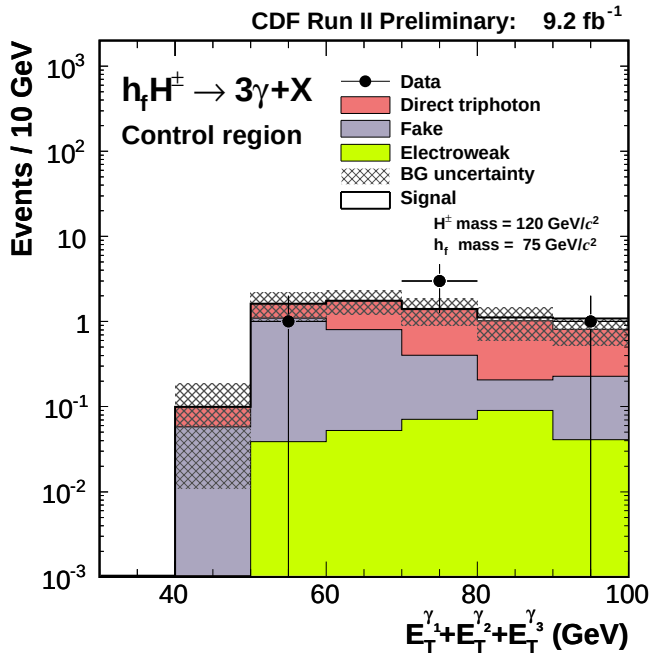

FIG. 19: Distributions of various sum of E_T for the $3\gamma + X$ events with $E_T^{\gamma 1} + E_T^{\gamma 2} < 90$ GeV and $E_T^{\gamma 3} < 24$ GeV, expected from the SM backgrounds and expected signal events for $m_{h_f} = 75$ and $m_{H^\pm} = 120$ GeV/c^2.

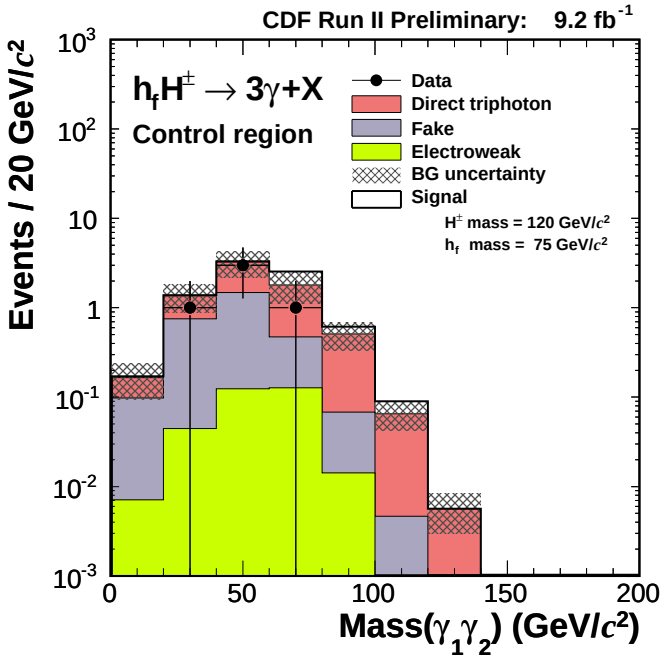

FIG. 20: Distributions of invariant mass of each pair of photons (the top two plots and bottom left plot) and three photons (the bottom right plot) for the $3\gamma+X$ events with $E_T^{\gamma 1} + E_T^{\gamma 2} < 90$ GeV and $E_T^{\gamma 3} < 24$ GeV, expected from the SM backgrounds and expected signal events for $m_{h_f} = 75$ and $m_{H^\pm} = 120$ GeV/c^2.

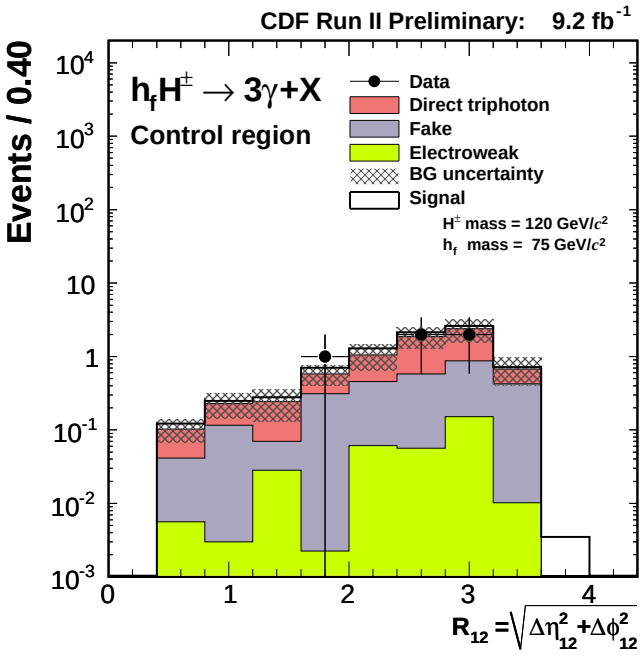

FIG. 21: Distributions of R (the distance in the η-ϕ plane between each pair of photons for the $3\gamma+X$ events with $E_T^{\gamma_1} + E_T^{\gamma_2} <$ 90 GeV and $E_T^{\gamma_3} < 24$ GeV, expected from the SM backgrounds and expected signal events for $m_{h_f} = 75$ and $m_{H^\pm} = 120$ GeV/c^2.

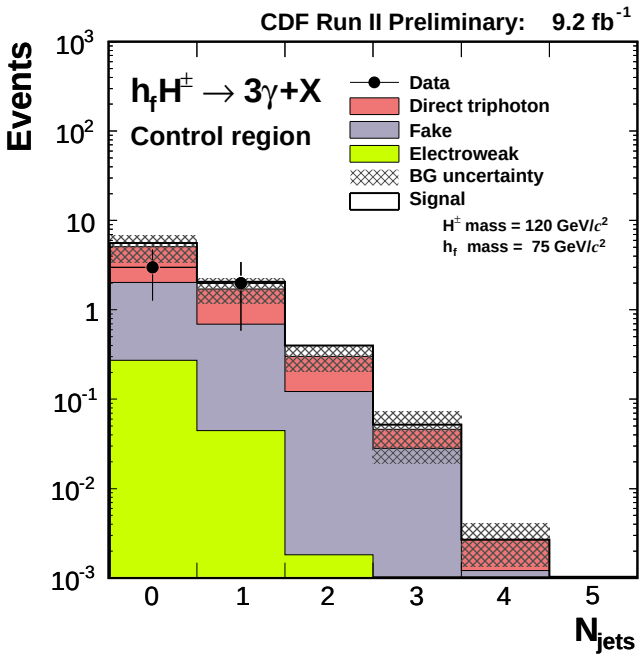

FIG. 22: The number of jets in the central region with $E_T > 10$ GeV for the $3\gamma + X$ events with $E_T^{\gamma_1} + E_T^{\gamma_2} < 90$ GeV and $E_T^{\gamma_3} < 24$ GeV, expected from the SM backgrounds and expected signal events for $m_{h_f} = 75$ and $m_{H^\pm} = 120$ GeV/c^2.

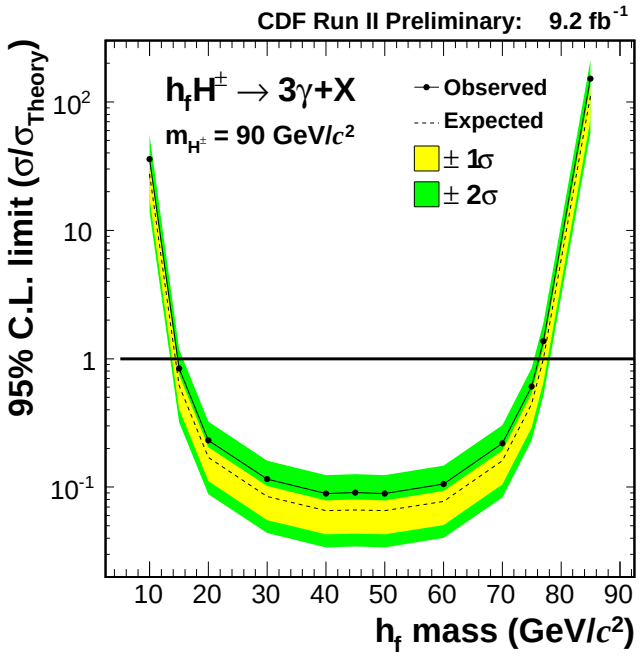

FIG. 23: The expected 95% C.L. cross section limits (solid lines) and theoretical cross sections (dashed lines) calculated for the case of applying $E_T^{\gamma 1} + E_T^{\gamma 2} > 90$ GeV.

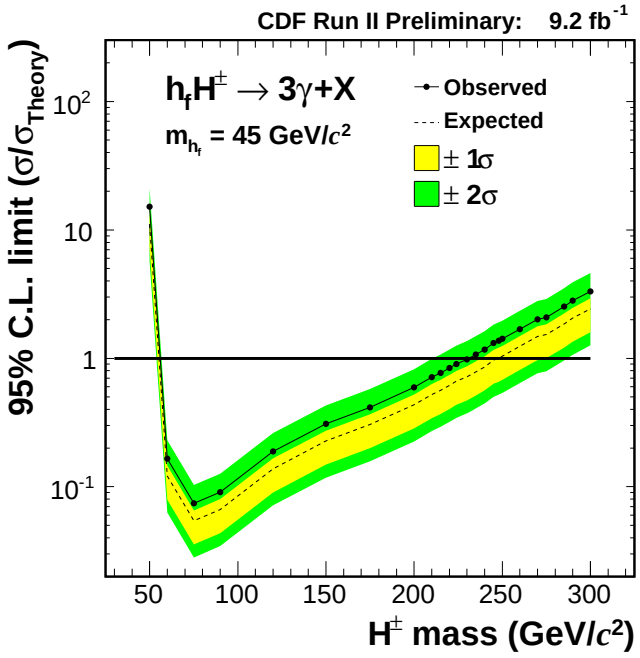

FIG. 24: The expected 95% C.L. cross section limits (solid lines) and theoretical cross sections (dashed lines) calculated for the case of applying $E_T^{\gamma 1} + E_T^{\gamma 2} > 90$ GeV.

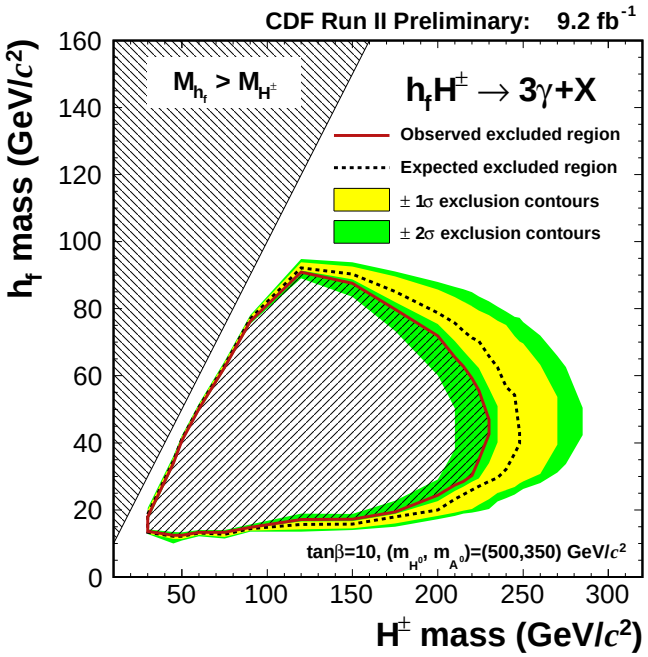

FIG. 25: The expected and observed 95% C.L. excluded mass region calculated for the case of applying $E_T^{\gamma 1} + E_T^{\gamma 2} > 90$ GeV.

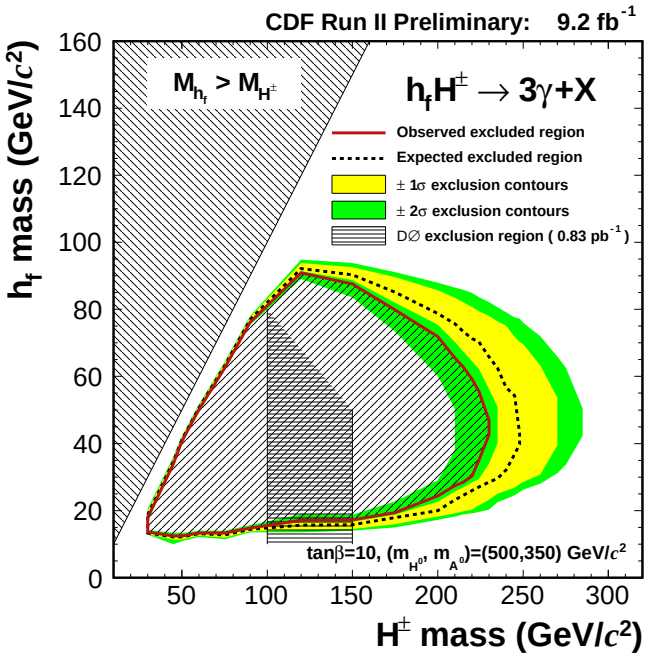

FIG. 26: The expected and observed 95% C.L. excluded mass region calculated for the case of applying $E_T^{\gamma 1} + E_T^{\gamma 2} > 90$ GeV. As a reference, the excluded h_f masses by the DØ analysis for $\tan\beta = 30$ is also shown in terms of two vertical lines. The shaded region between the lines are considered to be naturally excluded.

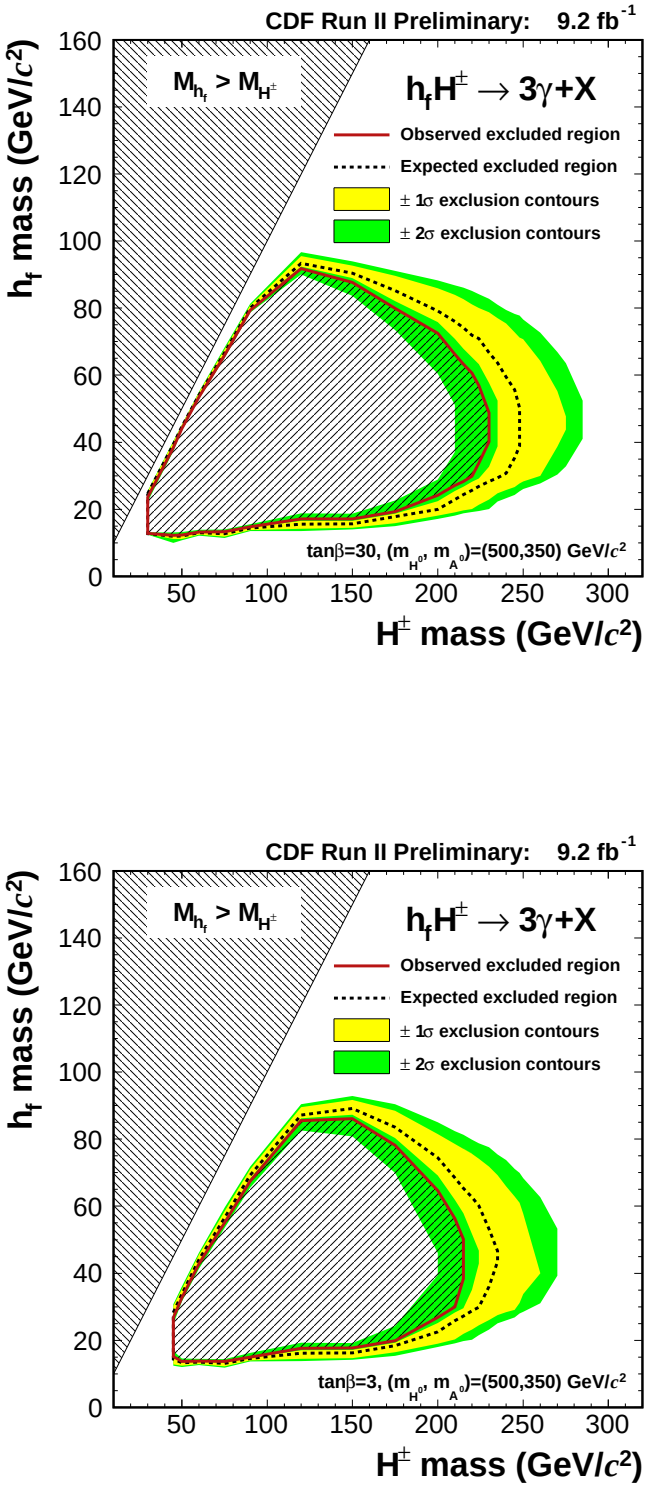

FIG. 27: The expected and observed 95% C.L. excluded mass region calculated for the case of applying $E_T^{\gamma 1} + E_T^{\gamma 2} > 90$ GeV. The top plot corresponds to $\tan\beta = 30$ and the bottom plot $\tan\beta = 3$.

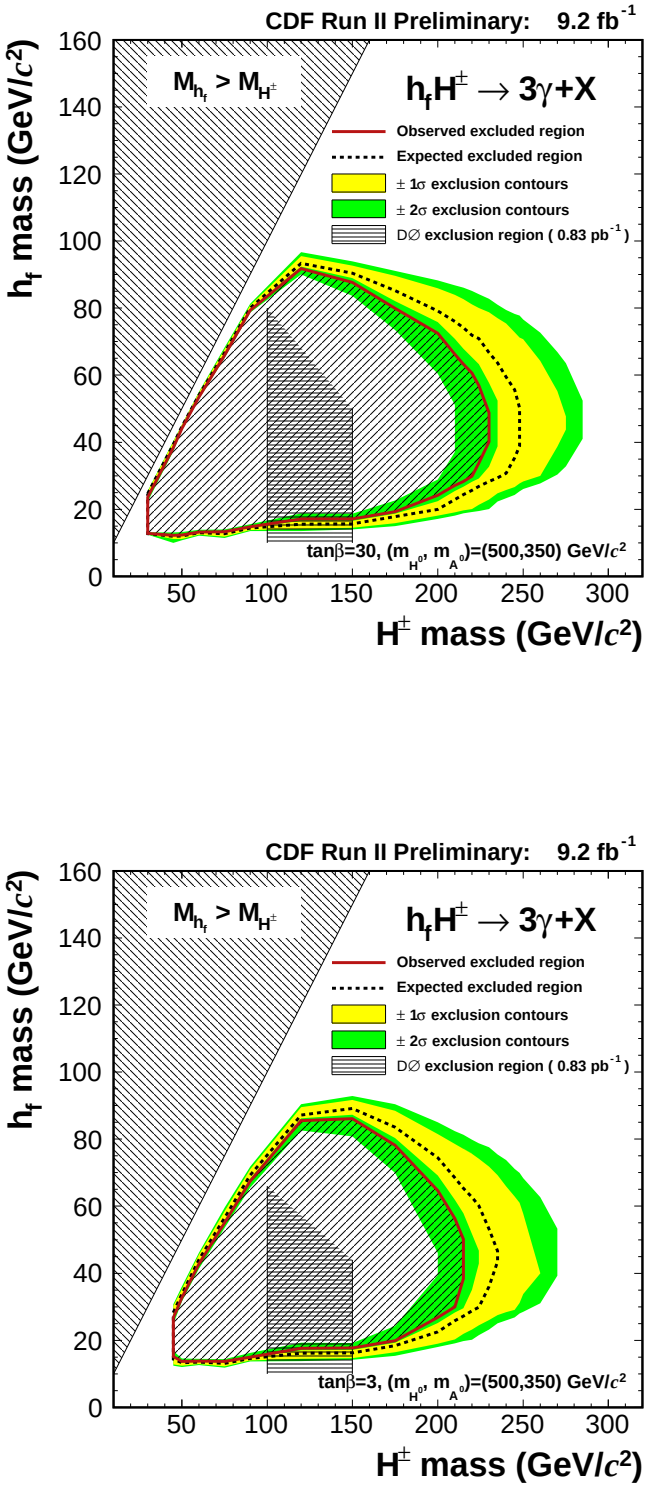

FIG. 28: The expected and observed 95% C.L. excluded mass region calculated for the case of applying $E_T^{\gamma 1} + E_T^{\gamma 2} > 90$ GeV. The top plot corresponds to $\tan\beta = 30$ and the bottom plot $\tan\beta = 3$. As a reference, the excluded h_f masses by the DØ analysis are also shown in terms of two vertical lines. The shaded region between the lines are considered to be naturally excluded.

Acknowledgments

We thank the Fermilab staff and the technical staffs of the participating institutions for their vital contributions. This work was supported by the U.S. Department of Energy and National Science Foundation; the Italian Istituto Nazionale di Fisica Nucleare; the Ministry of Education, Culture, Sports, Science and Technology of Japan; the Natural Sciences and Engineering Research Council of Canada; the National Science Council of the Republic of China; the Swiss National Science Foundation; the A.P. Sloan Foundation; the Bundesministerium für Bildung und Forschung, Germany; the Korean World Class University Program, the National Research Foundation of Korea; the Science and Technology Facilities Council and the Royal Society, UK; the Russian Foundation for Basic Research; the Ministerio de Ciencia e Innovación, and Programa Consolider-Ingenio 2010, Spain; the Slovak R&D Agency; the Academy of Finland; the Australian Research Council (ARC); and the EU community Marie Curie Fellowship contract 302103.

[1] ATLAS Collaboration, "Observation of a new particle in the search for the Standard Model Higgs boson with the ATLAS detector at the LHC", Phys. Lett. B716, 1 (2012); CMS Collaboration, "Observation of a new boson at a mass of 125 GeV with the CMS experiment at the LHC", Phys. Lett. B716, 30 (2012); CMS Collaboration, "Study of the Mass and Spin-Parity of the Higgs Boson Candidate via Its Decays to Z Boson Pairs", Phys. Rev. Lett. 110, 081803 (2013); ATLAS Collaboration, "Evidence for the spin-0 nature of the Higgs boson using ATLAS data", Phys. Lett. B726, 120 (2013);

[2] ATLAS Collaboration, "Evidence for Higgs Boson Decays to the $\tau^+\tau^-$ Final State with the ATLAS Detector", ATLAS-CONF-2013-108; CMS Collaboration, "Evidence for the direct decay of the 125 GeV Higgs boson to fermions", arXiv:1401.6527.

[3] H.E.Haber, G.L.Kane, and T.Sterling, Nucl. Phys. B161, 493 (1979).

[4] Sometimes called a "bosonic" or "bosophillic" Higgs boson as well.

[5] A. Stange, W.J. Marciano, and S. Willenbrock, Phys. Rev. D 49, 1354 (1994).

[6] M.A. Diaz and T.J. Weiler, hep-hp/9401259.

[7] V. Lemaitre for the ALEPH, DELPHI, L3, and OPAL collaborations, "Search for fermiophobic Higgs at LEP", Fundamental Interactions: Proceedings of the 20th Lake Louise Winter Institue, Canada, p199–203.

[8] The Tevatron New-Phenomena and Higgs Working Group for the CDF and DØ Collaborations, "Combined CDF and DØ Upper Limits on Fermiophobic Higgs Boson Production with up to 8.2 fb^{-1} of $p\bar{p}$ Data", arXiv:1302.1764, Supersymmetry 2011: 19th International Conference on Supersymmetry and Unification of Fundamental Interactions.

[9] ATLAS Collaboration, "Search for a fermiophobic Higgs boson in the diphoton decay channel with the ATLAS detector", Eur. Phys. J. C 72, 2157 (2012);
CMS Collaboration, "Searches for Higgs bosons in pp collisions at $\sqrt{s} = 7$ and 8 TeV in the context of four-generation and fermiophobic models", Phys. Lett. B 725, 36 (2013);

[10] A.G. Akeroyd and M.A. Díaz, Phys. Rev. D 67, 095007 (2003); A.G Akeroyd, A. Alves, M.A. Díaz, and O. Éboli, Eur. Phys. J. C48, 145 (2006).

[11] DØ Collaboration, "Search for Fermiophobic Higgs Boson in $3\gamma + X$ Events", DØ Note 5067-CONF.

[12] F. Abe, et al., Nucl. Instrum. Methods Phys. Res. A **271**, 387 (1988); D. Amidei, et al., Nucl. Instum. Methods Phys. Res. A **350**, 73 (1994); F. Abe, et al., Phys. Rev. D **52**, 4784 (1995); P. Azzi, et al., Nucl. Instrum. Methods Phys. Res. A **360**, 137 (1995); The CDFII Detector Technical Design Report, Fermilab-Pub-96/390-E

[13] http::/www.mcfm.fnal.gov

[14] S. Dawson, S.Dittmaier, and M. Spira, Phys. Rev. D 58, 115012 (1998).